

Linear instability analysis of a viscoelastic jet in a co-flowing gas stream

Zhaodong Ding^{1,2}, Kai Mu², Ting Si^{2,†} and Yongjun Jian¹

¹School of Mathematical Science, Inner Mongolia University, Hohhot, Inner Mongolia 010021, PR China

²Department of Modern Mechanics, University of Science and Technology of China, Hefei 230026, PR China

(Received 30 August 2021; revised 26 December 2021; accepted 11 January 2022)

The instability characteristic of a viscoelastic jet in a co-flowing gas stream is studied comprehensively. The important role of the non-uniform basic velocity in the instability analysis of viscoelastic jets is clarified, which first induces an unrelaxed elastic tension, and then produces a coupling term between the elastic tension and perturbation velocity. The elastic tension promotes the instability of the jet, while the coupling term exhibits a stabilizing effect, which is essentially related to the nonlinear constitutive relation of viscoelastic fluids and the non-uniform basic velocity. The competition between these two factors leads to the non-monotonic effect of fluid elasticity on the disturbance growth rate, which can be divided into two different regimes characterized by the Weissenberg number with values smaller or larger than unity. In different regimes, the structure of the eigenspectrum is also significantly different. Furthermore, three instability mechanisms are identified using the energy budget analysis, corresponding to the predominance of the surface tension, elastic tension and shear and pressure of the external gas, respectively. By analysing the variations of the growth rate and phase speed of the disturbances, the general features of viscoelastic jet instability are obtained. Finally, the transitions of instability modes in parameter spaces are investigated theoretically and the transition boundaries among them are provided. This study provides guidance for understanding the underlying mechanism of instability of a viscoelastic jet surrounded by a co-flowing gas stream and the transition criterion of different instability modes.

Key words: viscoelasticity, jets, multiphase flow

1. Introduction

The controllable production of microdroplets and microfibres from thin liquid jets is of great interest in various scientific and engineering applications, such as medicine,

† Email address for correspondence: tsi@ustc.edu.cn

pharmaceuticals, material science, chemistry, food, agriculture, textile, etc. (Gañán-Calvo *et al.* 2013). Capillary flows have been used to produce micro-jets effectively (Barrero & Loscertales 2007), where the interfaces of different fluid jets can be smoothly stretched to of the order of microns or less under the action of an external force field. As type of capillary flow, based on the flow focusing (FF) technique was proposed by Gañán-Calvo (1998), where a steady microscopic liquid jet is formed under the driving of an external high-speed co-flowing gas stream. FF has the advantage of producing a micron-level monodisperse spray, and has become a popular method of producing sub-millimetre jets through hydrodynamic means (Montanero & Gañán-Calvo 2020).

The research on the phenomenon of a liquid jet breaking into droplets has a history of more than a century since the pioneering work of Rayleigh (1878), where a temporal instability analysis of an inviscid liquid cylinder flowing with a uniform velocity was performed. The influence of the surrounding gas was neglected and surface tension was the only destabilizing factor. When the jet velocity is relatively small, Rayleigh's results are consistent with experiments, while for higher jet velocities, Rayleigh's results deviate from experiments. Weber (1931) found that the liquid viscosity has stabilizing effects, reducing the breakup rate and increasing the droplet size. Chandrasekhar (1961) proved that the mechanism of Rayleigh jet instability is capillary pinching. In the Rayleigh instability theory, the predicted droplet sizes are of the same order as the jet diameter. However, this theory cannot be applied to the atomization phenomenon which is the breakup of a liquid jet into droplets much smaller than the jet diameter. To explain the atomization process, Taylor (1962) took the gas density into account. He considered the limiting case of an infinitely thick jet and extremely small gas-to-liquid density ratio. Lin & Chen (1998) investigated the role of interfacial shear in the onset of instability of a cylindrical viscous liquid jet in a viscous gas surrounded by a coaxial circular pipe. They reported that the mechanism of the jet atomization is the shear and pressure fluctuation at the interface.

The instability and mode transition in FF have attracted more and more attention (Herrada *et al.* 2010; Guerrero *et al.* 2020; Mu *et al.* 2021). Rosell-Llompart & Gañán-Calvo (2008) distinguished two flow regimes in FF, which depend on the interaction between the liquid jet and the co-flowing gas stream (e.g. the Weber number We). For $1 < We < 20$, it is 'capillary FF', while for $We > 20$, it turns into 'turbulent FF'. Gordillo, Pérez-Saborid & Gañán-Calvo (2001) performed a linear temporal instability analysis of an inviscid jet and the co-flowing gas stream surrounding the jet, where the influences of the basic-velocity profiles of the liquid and gas are considered by solving the Navier–Stokes equations with the slenderness approximation. Their analysis in the case of a uniform liquid velocity profile recovered the classical Rayleigh inviscid result for well-developed and very thin gas boundary layers, but more importantly, the consideration of realistic liquid velocity profiles (i.e. non-uniform velocity profiles) revealed new families of modes which are essential to explain atomization experiments at large enough Weber numbers, and do not appear in the classical stability analysis of inviscid parallel streams.

It should be emphasized that many practical applications involve non-Newtonian viscoelastic jets, such as inkjet printing, micro/nano-fibre manufacture, spinning and electrospinning of polymeric solutions (Eggers & Villermaux 2008; Basaran, Gao & Bhat 2013; Alsharif, Uddin & Afzaal 2015; Li *et al.* 2019). The introduction of fluid elasticity can fundamentally modify the Newtonian flow dynamics. For example, the elasticity of fluid in high molecular polymer solutions may alter the linear amplification of disturbances in shear flows, shift the onset of laminar-to-turbulence transition and reduce drag in the turbulent flow regime (Page & Zaki 2016). In past decades, the instability of viscoelastic

jets has received widespread attention (Montanero & Gañán-Calvo 2008; Ponce-Torres *et al.* 2016; Ye, Yang & Fu 2016; Eggers, Herrada & Snoeijer 2020). However, in contrast to the large body of literature available on the study of Newtonian liquid jets, the theoretical work on the instability of viscoelastic jets is relatively limited due to the mathematical complexity in dealing with nonlinear rheological constitutive equations. Incipient research (e.g. Middleman 1965; Kroesser & Middleman 1969) that directly applied the linear stability theory to predict the axisymmetric breakup of viscoelastic jets did not achieve the same success as that with Newtonian fluid jets (Goldin *et al.* 1969; Gordon, Yerushalmi & Shinnar 1973). The linearized instability analysis predicted that a viscoelastic jet exhibits more rapid growth of axisymmetric wave disturbances than its Newtonian counterpart, implying that elasticity is a purely destabilizing factor for all unstable disturbances (Goldin *et al.* 1969; Liu & Liu 2006, 2008). This result does not agree with most experiments because viscoelastic jets generally take a longer time to break up into droplets than Newtonian ones (Gordon *et al.* 1973; Eggers & Villermaux 2008). In order to resolve this discrepancy between theoretical analysis and experimental observations, Goren & Gottlieb (1982) proposed that the liquid may be subject to an unrelaxed axial tension due to its prior history. Under the assumption that the stress relaxation time constant is sufficiently large, Goren & Gottlieb (1982) showed that the unrelaxed axial elastic tension can be a significant stabilizing influence.

However, there are some inherent limitations in Goren & Gottlieb's theory. First of all, the unrelaxed axial elastic tension is artificially specified (Ruo *et al.* 2011; Mohamed *et al.* 2015; Xie *et al.* 2016), and its real physical meaning is unclear. Secondly, the elastic tension decays exponentially with an increase in the distance from the nozzle. In order to maintain an approximate constant elastic tension, some constraints need to be imposed. For example, the validity of this assumption requires that the distance over which the velocity profile relaxes completely from the nozzle is much shorter than the distance corresponding to the elastic stress relaxation (Ruo *et al.* 2011). In the present study, we try to clarify the physical meaning of the unrelaxed elastic tension and remove unnecessary constraints through comprehensive and detailed investigation.

It is generally believed that when linear stability theory is used to study the mechanism of jet breakup, two primary conditions need to be satisfied to get results consistent with experiments: one is that the model must include all important parameters, such as viscosity, density, surface tension, etc.; the other is that the basic flow should be the same as or similar to the real flow. In specific research of FF, when the physical model is close to the actual situation, temporal stability analysis often gives results comparable to experiments (Si *et al.* 2009). In the linear stability analysis of co-flowing liquid–gas jets performed by Gordillo *et al.* (2001), the consideration of realistic (non-uniform) basic velocity profiles revealed new families of modes which are essential to explain atomization experiments at large enough Weber numbers. We are surprised to see that almost all the previous studies adopted uniform velocity profiles in the linear stability analysis of viscoelastic jets, probably for the sake of mathematical simplicity. In this work, the temporal linear instability analysis is performed by considering viscoelastic jets with non-uniform basic-velocity profiles in the FF flow configuration. The liquid is assumed to be an Oldroyd-B viscoelastic fluid, which was commonly used in previous studies. The characteristic of an Oldroyd-B fluid is that its viscosity is independent of shear in flow and elastic effects can be clearly distinguished from the viscous effects. It has turned out to be an appropriate model in describing the viscoelasticity of dilute polymer solutions under small or moderate deformation (Larson 1992; Morozov & van Saarloos 2007; James 2009).

The paper is organized as follows. Section 2 provides the governing equations for viscoelastic jets, the base-state velocity profile and stress tensor and the validation of the numerical method used in this study. In § 3, an energy budget analysis is implemented to access the dominating forces in the instability analysis of viscoelastic jets. In § 4, the influence of fluid elasticity on the jet instability is discussed in detail in § 4.1, where three different instability mechanisms can be identified by means of the energy budget analysis. Section 4.2 demonstrates the general features of instability modes by examining the variations of the maximum growth rate and the corresponding phase speed. In § 4.3, we investigate the transitions of instability modes in parameter spaces and provide the transition boundaries between different modes. Finally, the study is summarized and concluded in § 5.

2. Theoretical model and numerical method

2.1. Governing equations

Consider the linear instability of an incompressible viscoelastic liquid jet of radius R_1 and density ρ_1 . The jet is surrounded by a viscous gas in an external environment, and the gas stream is considered as a cylinder of radius R_2 with the outside surface being assumed to slip. The effects of gravity and temperature are negligible. Only the axisymmetric disturbance is considered. The theoretical model is sketched in figure 1, where a cylindrical polar coordinate system is used with r , θ and z denoting the radial, azimuthal and axial directions. The characteristic scales used for non-dimensionalizing the governing equations are: radius R_1 for lengths, base-flow velocity U_0 at the centre for velocities, R_1/U_0 for time and $\rho_1 U_0^2$ for pressures and stresses.

The dimensionless continuity and Cauchy momentum equations for the viscoelastic liquid are given by

$$\nabla \cdot V_1 = 0, \quad \frac{\partial V_1}{\partial t} + (V_1 \cdot \nabla) V_1 = -\nabla p_1 + \nabla \cdot T. \quad (2.1a,b)$$

Here, $V_1 = v_1 e_r + w_1 e_\theta + u_1 e_z$ is the velocity field, p_1 is the pressure field and T is the deviatoric stress tensor, which can be decomposed into a polymer contribution T_p and a Newtonian solvent contribution T_s , i.e. $T = T_s + T_p$. The total viscosity of the solution is the sum of the solvent and polymer contributions, i.e. $\mu_1 = \mu_s + \mu_p$, with μ_s and μ_p being the solvent and polymer viscosities, respectively. The solvent to solution viscosity ratio is denoted by $X = \mu_s/\mu_1$; $X = 1$ recovers the Newtonian limit. The dimensionless constitutive equation for the Newtonian solvent stress T_s is

$$T_s = \frac{X}{Re} [\nabla V_1 + (\nabla V_1)^T], \quad (2.2)$$

while the polymer stress satisfies the Oldroyd-B constitutive relation (Bird, Armstrong & Hassager 1987; Larson 1988)

$$T_p + Wi T_p^\nabla = \frac{1-X}{Re} [\nabla V_1 + (\nabla V_1)^T], \quad (2.3)$$

where the superscripts T and ∇ denote transpose and the upper-convected derivative defined by

$$T_p^\nabla = \frac{\partial T_p}{\partial t} + V_1 \cdot \nabla T_p - (\nabla V_1)^T \cdot T_p - T_p \cdot \nabla V_1. \quad (2.4)$$

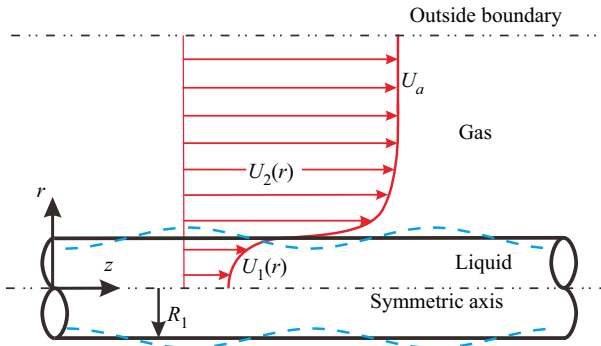


Figure 1. Schematic diagram of the theoretical model of viscoelastic jets.

For a fixed X , the dimensionless groups relevant to the stability of the Oldroyd-B fluid are the Reynolds number $Re = \rho_1 U_0 R_1 / \mu_1$, the Weber number $We = \rho_1 U_0^2 R_1 / \sigma$, representing the ratio of inertial force to surface tension (σ), and the Weissenberg number $Wi = \lambda U_0 / R_1$, which is the ratio of the polymer relaxation time λ to the flow time scale. Alternatively, the elasticity number, $El = Wi / Re = \lambda \mu_1 / \rho_1 R_1^2$, can be introduced, which represents the ratio of the elastic and viscous time scales of the liquid jet (Brenn, Liu & Durst 2000). The advantage of El is that its value is determined by the physical properties of the fluid itself and has nothing to do with the velocity. Obviously, when $El = 0$ (or equivalently $Wi = 0$), the model degenerates to the Newtonian fluid. On the other hand, if all nonlinear terms in (2.4) disappear, the Jeffreys constitutive relation (a linear viscoelastic model) is obtained as follows:

$$\mathbf{T}_p + Wi \frac{\partial \mathbf{T}_p}{\partial t} = \frac{1 - X}{Re} [\nabla V_1 + (\nabla V_1)^T]. \quad (2.5)$$

To facilitate expression of the nonlinear terms in the constitutive equation, we define an operation

$$\langle \mathbf{T}_p, V_1 \rangle \equiv V_1 \cdot \nabla \mathbf{T}_p - (\nabla V_1)^T \cdot \mathbf{T}_p - \mathbf{T}_p \cdot \nabla V_1, \quad (2.6)$$

which is bilinear and represents the coupling interaction between the polymer stress and the velocity. Using this notation, the upper-convected derivative can be rewritten as

$$\overset{\nabla}{\mathbf{T}}_p = \frac{\partial \mathbf{T}_p}{\partial t} + \langle \mathbf{T}_p, V_1 \rangle. \quad (2.7)$$

The dimensionless governing equations for the ambient gas with density ρ_2 and viscosity μ_2 are given by

$$\nabla \cdot V_2 = 0, \quad \frac{\partial V_2}{\partial t} + (V_2 \cdot \nabla) V_2 = -\frac{1}{Q} \nabla p_2 + \frac{N}{Q Re} \nabla^2 V_2, \quad (2.8a,b)$$

where $V_2 = v_2 \mathbf{e}_r + w_2 \mathbf{e}_\theta + u_2 \mathbf{e}_z$ is the velocity field, p_2 is the pressure field, $Q = \rho_2 / \rho_1$ and $N = \mu_2 / \mu_1$ are the density ratio and the viscosity ratio, respectively.

To close the system, consistent conditions at the symmetry axis $r = 0$ and the outside boundary $r = a$ with $a = R_2/R_1$ are needed

$$\left. \begin{aligned} v_1 = \frac{\partial u_1}{\partial r} = \frac{\partial p_1}{\partial r} = 0, \quad \text{at } r = 0, \\ v_2 = \frac{\partial u_2}{\partial r} = \frac{\partial p_2}{\partial r} = 0, \quad \text{at } r = a. \end{aligned} \right\} \quad (2.9)$$

At the liquid–gas interface $r = h(z, t)$, the continuity of velocity, and the kinematic and dynamic conditions are satisfied, i.e.

$$V_1 = V_2, \quad (2.10a)$$

$$v_1 = \left(\frac{\partial}{\partial t} + V_1 \cdot \nabla \right) h, \quad (2.10b)$$

$$(T_2 - T_1) \cdot \mathbf{n} = \frac{1}{We} (\nabla \cdot \mathbf{n}) \mathbf{n}, \quad (2.10c)$$

where $T_1 = -p_1\mathbf{I} + T_s + T_p$ and $T_2 = -p_2\mathbf{I} + N/Re[\nabla V_2 + (\nabla V_2)^T]$ with \mathbf{I} the unit tensor and where \mathbf{n} is the outward unit vector normal to the interface.

2.2. Basic-velocity profile and stress tensor

The first step in performing the stability analysis is to find the basic velocity profiles for the liquid and gas streams. In order to get reasonable results, the basic flow should be the same as or similar to the real flow, as stated in the introduction section. Lin & Ibrahim (1990) derived an analytical velocity profile satisfying the Navier–Stokes equations in their study on the instability of a cylindrical Newtonian fluid jet encapsulated by a viscous gas in a vertical circular pipe. Gordillo *et al.* (2001) obtained the velocity profiles in the FF jet problem by numerically solving the boundary-layer equations. For given initial velocity profiles of liquid and gas, the evolution of the liquid and gas streams in space can be computed. However, the algebraic operation is complicated. On the other hand, several approximate velocity profiles have been successfully applied in theoretical analysis compared with the experimental results, e.g. that of the error function (Yecko, Zaleski & Fullana 2002) and that of the hyperbolic–tangent function (Sevilla, Gordillo & Martínez-Bazán 2002; Gañán-Calvo & Riesco-Chueca 2006; Si *et al.* 2009). In this work, velocity profiles of the hyperbolic–tangent function in the two fluids are utilized. The basic velocity is assumed to be axisymmetric and unidirectional, and denoted by $U_i = [0, 0, U_i(r)]$, where the subscripts $i = 1, 2$ stand for the liquid and the gas, respectively.

The dimensionless form $U_i(r)$, similar to that of Si *et al.* (2009), is selected as

$$U_i(r) = a_i \tanh(b_i(r - 1)) + d_i, \quad (2.11)$$

where a_i, b_i and $d_i (i = 1, 2)$ are the coefficients to be determined. Using the following constraint conditions: (i) continuity of the velocity and shear stress at the jet interface; (ii) symmetry of the velocity at the symmetric axis; (iii) uniformity of the velocity at the

	Goren & Gottlieb's theory	Present result
Expression	$\bar{\tau}_{zz}(z) = \bar{\tau}_a \exp(-z/\lambda U)$	$\Gamma_{zz} = 2(1 - X)El U_1^2$
Basic-velocity profile	Uniform	Non-uniform
Parameters	Artificial assumption	Practical significance
Requirement	$\lambda U/l \gg 1$	None

Table 1. Comparison of our result with Goren & Gottlieb's theory.

outside boundary, the basic velocities can be written as (Si *et al.* 2009)

$$U_1(r) = (U_s - 1) \tanh \left[\frac{K}{U_s - 1} (r - 1) \right] + U_s, \quad (2.12a)$$

$$U_2(r) = (U_a - U_s) \tanh \left[\frac{K}{N(U_a - U_s)} (r - 1) \right] + U_s, \quad (2.12b)$$

where U_s is the velocity at the unperturbed interface ($r = 1$), U_a is the velocity at the outside boundary ($r = a$) and K is the slope of the liquid velocity profile at the interface. The parameter K characterizes the strength of interfacial shear. A large value of K implies a strong interfacial shear. When $K = 0$, one can get a uniform velocity profile in the whole flow field. In FF, the gas-to-liquid momentum ratio is very close to unity, and thus $U_a \approx Q^{-1/2}$ (see Si *et al.* 2009), which is also used in this work.

Under the assumption of a steady-state axisymmetric and non-uniform basic velocity, the polymer contribution to the stress tensor in the base state can be obtained by solving (2.3) and (2.4), as follows:

$$\boldsymbol{\Gamma} = \begin{bmatrix} \Gamma_{rr} & 0 & \Gamma_{rz} \\ 0 & \Gamma_{\theta\theta} & 0 \\ \Gamma_{zr} & 0 & \Gamma_{zz} \end{bmatrix} = \frac{1 - X}{Re} \begin{bmatrix} 0 & 0 & U_1' \\ 0 & 0 & 0 \\ U_1' & 0 & 2WiU_1^2 \end{bmatrix}, \quad (2.13)$$

where $f' \equiv df/dr$. Note that there is a non-zero tension Γ_{zz} along the streamlines proportional to the square of the velocity gradient, which does not appear for both Newtonian and linear viscoelastic models (i.e. the Jeffreys model). Thus, unlike the Newtonian and Jeffreys counterparts, the Oldroyd-B fluid exhibits a non-zero first normal stress difference ($\Gamma_{zz} - \Gamma_{rr}$). Most notably, Γ_{zz} plays the role of unrelaxed axial elastic tension, compared with Goren & Gottlieb's theory, but the source of unrelaxed elastic tension is completely different. In Goren & Gottlieb's theory, the axial elastic tension was obtained by integrating (2.3) and (2.4) based on a uniform basic velocity U , i.e. $\bar{\tau}_{zz}(z) = \bar{\tau}_a \exp(-z/\lambda U)$ (see (2.6) in Ruo *et al.* 2011), where $\bar{\tau}_a$ is the axial tension at the nozzle exit and its magnitude needs to be specified artificially. In addition, Goren & Gottlieb's theory requires $\lambda U/l \gg 1$, with l being the wavelength of a disturbance, so that the mathematical terms involving the spatial gradient of the tension can be negligible over distances comparable to the characteristic wavelength (Ruo *et al.* 2011). As a contrast, by using a non-uniform basic velocity, we get the axial elastic tension $\Gamma_{zz} = 2(1 - X)El U_1^2$, which is a function of r and related to the velocity gradient, elasticity number and solvent viscosity ratio. Note that no additional assumptions need to be introduced in our situation and the physical meaning of unrelaxed elastic tension is clear. A comparison of our result with Goren & Gottlieb's theory is summarized in table 1.

2.3. Linear stability analysis

To carry out the linear stability analysis, the base state is subjected to small amplitude axisymmetric disturbances as follows:

$$V_i = U_i + \tilde{V}_i, \tag{2.14a}$$

$$p_i = P_i + \tilde{p}_i, \tag{2.14b}$$

$$T_p = \Gamma + \tilde{T}_p. \tag{2.14c}$$

For axisymmetric disturbances, the perturbation velocity and elastic stress tensor are

$$\tilde{V}_i = \begin{bmatrix} \tilde{v}_i \\ 0 \\ \tilde{u}_i \end{bmatrix} \quad \text{and} \quad \tilde{T}_p = \begin{bmatrix} \tilde{\tau}_{rr} & 0 & \tilde{\tau}_{rz} \\ 0 & \tilde{\tau}_{\theta\theta} & 0 \\ \tilde{\tau}_{zr} & 0 & \tilde{\tau}_{zz} \end{bmatrix}, \tag{2.15a,b}$$

respectively. It is worth noting that, although axisymmetric disturbances are considered, the inclusion of the component $\tilde{\tau}_{\theta\theta}$ in the elastic stress tensor is necessary because the constitutive equation of $\tilde{\tau}_{\theta\theta}$ is related to the perturbation velocity \tilde{v}_1 , which is non-zero (see (A2) and (A6) in Appendix A).

Substituting (2.14) into the governing equations (2.1a,b)–(2.3) and (2.8a,b) and neglecting high-order terms, we obtain the governing equations for disturbances as follows:

$$\nabla \cdot \tilde{V}_1 = 0, \tag{2.16}$$

$$\frac{\partial \tilde{V}_1}{\partial t} + (\tilde{V}_1 \cdot \nabla) U_1 + (U_1 \cdot \nabla) \tilde{V}_1 = -\nabla \tilde{p}_1 + \nabla \cdot \tilde{T}_s + \nabla \cdot \tilde{T}_p, \tag{2.17}$$

$$\tilde{T}_s = \frac{X}{Re} \left[\nabla \tilde{V}_1 + (\nabla \tilde{V}_1)^T \right], \tag{2.18}$$

$$\tilde{T}_p + Wi \left[\frac{\partial \tilde{T}_p}{\partial t} + \langle \tilde{T}_p, U_1 \rangle + \langle \Gamma, \tilde{V}_1 \rangle \right] = \frac{1-X}{Re} \left[\nabla \tilde{V}_1 + (\nabla \tilde{V}_1)^T \right], \tag{2.19}$$

$$\nabla \cdot \tilde{V}_2 = 0, \tag{2.20}$$

$$\frac{\partial \tilde{V}_2}{\partial t} + (\tilde{V}_2 \cdot \nabla) U_2 + (U_2 \cdot \nabla) \tilde{V}_2 = -\frac{1}{Q} \nabla \tilde{p}_2 + \frac{N}{Q} \frac{1}{Re} \nabla^2 \tilde{V}_2, \tag{2.21}$$

in which the coupling terms $\langle \tilde{T}_p, U_1 \rangle$ and $\langle \Gamma, \tilde{V}_1 \rangle$ are defined in the same way as in (2.6).

Using the normal mode method, the perturbation quantities (velocity, pressure and elastic stress) can be represented in the form of Fourier modes in the following manner:

$$\tilde{f}(r, z, t) = \hat{f}(r) \exp\{ik(z - ct)\}, \tag{2.22}$$

where k is the dimensionless axial wavenumber and $c = c_r + ic_i$ is the dimensionless complex wave speed. The flow is temporally unstable (stable) if $c_i > 0$ (< 0). Let $s = kc_i$ denote the growth rate of a disturbance if it is unstable, and c_r represent the phase speed of the disturbance. The perturbed interface can be expressed as

$$h(z, t) = 1 + \tilde{\eta}(z, t) \quad \text{with} \quad \tilde{\eta}(z, t) = \hat{\eta} \exp\{ik(z - ct)\}. \tag{2.23}$$

Substituting the forms (2.22) of the perturbation quantities into the governing equations (2.16)–(2.21), one can obtain a set of governing equations for the perturbation amplitudes, which are presented with the corresponding boundary conditions in Appendix A.

2.4. Numerical method

The governing equations (A1)–(A10) together with the boundary conditions (A11)–(A17) in Appendix A form an eigenvalue problem. Obviously, it is difficult to determine the exact spectrum since an explicit dispersion relation is not available, even for the axisymmetric case. In previous studies, the Chebyshev spectral collocation method has been successfully applied to this type of problem because of its ability in identifying all eigenvalues with high accuracy and efficiency (Boyd 1999; Weideman & Reddy 2000; Chaudhary *et al.* 2021). We employ this method to determine the complex eigenvalue (c), where the dynamical variables (velocity, pressure and stress perturbations) are expanded as a finite sum of Chebyshev polynomials and substituted in the above linearized differential equations. The liquid region $r \in [0, 1]$ is mapped into the computational space $y \in [-1, 1]$ through the linear transformation

$$r = \frac{1 + y}{2}, \tag{2.24}$$

and the gas region $r \in [1, a]$ is mapped into the computational space $y \in [-1, 1]$ through

$$r = \frac{y(1 - a) + (1 + a)}{2}. \tag{2.25}$$

In our spectral formulation, we discretize all of the equations (A1)–(A10), and the resulting generalized eigenvalue problem is of the form

$$\mathbf{A}\mathbf{x} = c\mathbf{B}\mathbf{x}, \tag{2.26}$$

where the coefficient matrices \mathbf{A} and \mathbf{B} are obtained from the governing equations and the boundary conditions, and $\mathbf{x} = [\mathbf{x}_1; \mathbf{x}_2; \hat{\eta}]$ with $\mathbf{x}_1 = (\hat{v}_1, \hat{u}_1, \hat{p}_1, \hat{\tau}_{rr}, \hat{\tau}_{rz}, \hat{\tau}_{\theta\theta}, \hat{\tau}_{zz})^T$ and $\mathbf{x}_2 = (\hat{v}_2, \hat{u}_2, \hat{p}_2)^T$ being the vectors comprising of the coefficients of the spectral expansion at the collocation points in liquid and gas regions, respectively. The size of the coefficient matrices is $(7N_1 + 3N_2 + 11) \times (7N_1 + 3N_2 + 11)$, where $N_1 + 1$ and $N_2 + 1$ are the numbers of Gauss–Lobatto collocation points in liquid and gas regions, respectively.

A MATLAB code is developed to solve the generalized eigenvalue problem (2.26). The numbers of collocation points are chosen to satisfy the desired accuracy. The convergence of the complex wave speed (c) to the numbers of the collocation points N_1 and N_2 for different El is illustrated in table 2. It can be seen that, as El increases, more collocation points are needed in order to achieve the desired accuracy. A further increase in El (i.e. $El > 10$ and $X = 0.9$) will lead to a sharp deterioration in convergence, which can be explained by means of the behaviour of unstable eigenvalues with El (see figure 15 in Appendix B). To avoid this problem, we restrict ourselves to the range of $(1 - X)El < 1$ in this work. For fixed El and X , the effects of the collocation points and the radius ratio a on the convergence are shown in table 3. In the calculations, $a = 7$, $N_1 = 30$ and $N_2 = 40$ provide the complex wave speed with a more than three-digit accuracy. Therefore, such a set of (a, N_1, N_2) will be used in our calculations, but when higher accuracy is required, like the calculations of eigenspectra, we must resort to more collocation points (see figures 13–15). The validity of the code has been checked by comparing with the result of Si *et al.* (2009) in the Newtonian limit case and that of Ruo *et al.* (2011) in the case of viscoelastic jets with uniform basic-velocity profiles, as illustrated in figure 2.

3. Energy budget

Energy budget is an elaborate method to access the mechanism of jet instability (Lin 2003; Li, Yin & Yin 2011; Ye *et al.* 2016). A history of the use of energy budgets can

El	N_1	N_2	c_r	c_i
0.1	20	60	1.191925	0.306297
0.1	30	60	1.191925	0.306297
2	20	60	1.091806	0.189093
2	40	60	1.091803	0.189093
8	20	60	1.065633	0.018524
8	60	60	1.065416	0.018358
8	90	60	1.065416	0.018358

Table 2. Convergence of the complex wave speed for different El , where $Re = 100$, $We = 3$, $X = 0.9$, $Q = 0.0013$, $N = 0.018$, $K = 0.9$, $U_s = 1.2$, $a = 4$ and $k = 1$.

a	N_1	N_2	c_r	c_i
3	20	40	1.144541	0.233055
4	20	40	1.138434	0.227604
5	30	40	1.137637	0.226885
5	30	60	1.137637	0.226885
6	30	40	1.137533	0.226791
7	30	40	1.137519	0.226779

Table 3. Convergence of the complex wave speed for different radius ratios a , where $Re = 100$, $We = 3$, $El = 1$, $X = 0.9$, $Q = 0.0013$, $N = 0.018$, $K = 0.9$, $U_s = 1.2$ and $k = 1$.

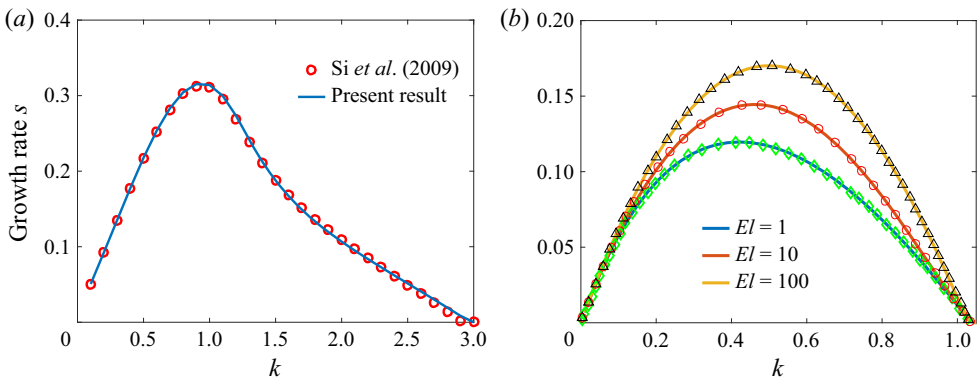


Figure 2. Variations of the growth rate s as a function of the dimensionless axial wavenumber k . (a) Compared with the results of Si *et al.* (2009) in the Newtonian limit ($El \rightarrow 0$), where $El = 0.01$, $Re = 100$, $We = 3$, $X = 0.9$, $Q = 0.0013$, $N = 0.018$, $K = 1$, $U_s = 1.2$, $a = 5$; (b) compared with the results of Ruo *et al.* (2011) in the case of viscoelastic jets with the uniform basic-velocity profile and inviscid ambient gas under the same parameters (see figure 1 in Ruo *et al.* (2011); note that they used De instead of El there), where the symbols represent the results of Ruo *et al.* (2011) and the curves are the results of our calculations.

be found in Joseph & Renardy (1992). The common procedure is to represent the rate of change of disturbance kinetic energy as a sum of the rates of various terms, such as the works of viscosity and surface tension (Otto, Rossi & Boeck 2013; Qiao *et al.* 2020; Mu *et al.* 2021). To better understand the role of liquid elasticity in jet instability, we perform such an energy analysis. First, taking a dot product of the linearized momentum equation (2.17) with the disturbance velocity \tilde{V}_1 , and then integrating over a control volume of one

disturbance wavelength $\Lambda = 2\pi/k$, we get

$$\begin{aligned} \iiint_{\substack{0 \leq z \leq \Lambda \\ 0 \leq r \leq 1}} (\partial_t + \mathbf{U}_1 \cdot \nabla) e \, dV = & - \iiint_{\substack{0 \leq z \leq \Lambda \\ 0 \leq r \leq 1}} \tilde{\mathbf{V}}_1 \cdot (\tilde{\mathbf{V}}_1 \cdot \nabla \mathbf{U}_1) \, dV - \iint_S \tilde{p}_1 \tilde{\mathbf{V}}_1 \cdot \mathbf{n} \, dS \\ & + \iiint_{\substack{0 \leq z \leq \Lambda \\ 0 \leq r \leq 1}} \tilde{\mathbf{V}}_1 \cdot (\nabla \cdot \tilde{\mathbf{T}}_s) \, dV + \iiint_{\substack{0 \leq z \leq \Lambda \\ 0 \leq r \leq 1}} \tilde{\mathbf{V}}_1 \cdot (\nabla \cdot \tilde{\mathbf{T}}_p) \, dV, \end{aligned} \quad (3.1)$$

where $e = \tilde{\mathbf{V}}_1 \cdot \tilde{\mathbf{V}}_1/2$ is the disturbance kinetic energy, S is the surface of the control volume and \mathbf{n} denotes the outward-pointing unit normal vector of the surface. Noting that $\tilde{\mathbf{V}}_1 \cdot \nabla \tilde{p}_1 = \nabla \cdot (\tilde{p}_1 \tilde{\mathbf{V}}_1)$ because of the incompressibility, the divergence theorem has been applied to the second term on the right-hand side of (3.1).

The term on the left-hand side of (3.1) represents the rate of change of the disturbance kinetic energy. The first term on the right-hand side gives the rate of energy transfer between the basic flow and the disturbance. The second term gives the rate of work done by the pressure. The third and fourth terms on the right-hand side of (3.1) can be further rewritten by means of the formulas (White 1998)

$$\tilde{\mathbf{V}}_1 \cdot (\nabla \cdot \tilde{\mathbf{T}}_s) = \nabla \cdot (\tilde{\mathbf{V}}_1 \cdot \tilde{\mathbf{T}}_s) - \tilde{\mathbf{T}}_s : \nabla \tilde{\mathbf{V}}_1, \quad (3.2a)$$

$$\tilde{\mathbf{V}}_1 \cdot (\nabla \cdot \tilde{\mathbf{T}}_p) = \nabla \cdot (\tilde{\mathbf{V}}_1 \cdot \tilde{\mathbf{T}}_p) - \tilde{\mathbf{T}}_p : \nabla \tilde{\mathbf{V}}_1. \quad (3.2b)$$

Thus, (3.1) can be rewritten as

$$\begin{aligned} \iiint_{\substack{0 \leq z \leq \Lambda \\ 0 \leq r \leq 1}} (\partial_t + \mathbf{U}_1 \cdot \nabla) e \, dV = & - \iiint_{\substack{0 \leq z \leq \Lambda \\ 0 \leq r \leq 1}} \tilde{\mathbf{V}}_1 \cdot (\tilde{\mathbf{V}}_1 \cdot \nabla \mathbf{U}_1) \, dV \\ & + \iint_S \left[-\tilde{p}_1 \tilde{\mathbf{V}}_1 + \tilde{\mathbf{V}}_1 \cdot (\tilde{\mathbf{T}}_s + \tilde{\mathbf{T}}_p) \right] \cdot \mathbf{n} \, dS \\ & - \iiint_{\substack{0 \leq z \leq \Lambda \\ 0 \leq r \leq 1}} \tilde{\mathbf{T}}_s : \nabla \tilde{\mathbf{V}}_1 \, dV - \iiint_{\substack{0 \leq z \leq \Lambda \\ 0 \leq r \leq 1}} \tilde{\mathbf{T}}_p : \nabla \tilde{\mathbf{V}}_1 \, dV. \end{aligned} \quad (3.3)$$

After substituting the dynamic boundary conditions (A15) and (A16) into the second term on the right-hand side of (3.3) in order to include the influence of interface movement, we can finally write the energy budget as

$$\text{KE} = \text{REY} + \text{PRG} + \text{NVG} + \text{SHG} + \text{SUT} + \text{SHB} + \text{NE} + \text{DIS} + \text{DIP}, \quad (3.4)$$

where the expression of each term and its physical interpretation are summarized in table 4. It is notable that there are two important terms (i.e. NE and DIP) related to the elastic effect in the energy budget analysis, which are absent for Newtonian jets. Furthermore, for the terms of surface integral in (3.4), such as PRG, NVG, SHG, SUT, SHB and NE, the integrals over the two ends (i.e. $z = 0$ and $z = \Lambda$) of the control volume cancel each other out because the disturbance is periodic in the z -direction, and the surface integral is only related to the integral over the side of the control volume (i.e. $r = 1$).

Because of the non-uniqueness of eigenfunction for the eigenvalue problem (2.26), it leads to the non-uniqueness of all energy terms in (3.4). To eliminate this problem, it is

Term	Physical interpretation
$KE = \pi \int_0^A \int_0^1 (\partial_t + U_1 \partial_z)(\tilde{v}_1^2 + \tilde{u}_1^2) r dr dz$	Rate of change of the disturbance kinetic energy
$REY = -2\pi \int_0^A \int_0^1 U_1' \tilde{u}_1 \tilde{v}_1 r dr dz$	Energy exchange between the disturbance and basic flow
$PRG = -2\pi \int_0^A (\tilde{p}_2 \tilde{v}_1)_{r=1} dz$	Rate of work done by the gas pressure fluctuation on the liquid jet
$NVG = \frac{4N\pi}{Re} \int_0^A (\tilde{v}_1 \partial \tilde{v}_2 / \partial r)_{r=1} dz$	Rate of work done by the normal viscous stress exerted by the fluctuating gas at the interface
$SHG = \frac{2N\pi}{Re} \int_0^A [\tilde{u}_1 (\partial \tilde{u}_2 / \partial r + \partial \tilde{v}_2 / \partial z)]_{r=1} dz$	Rate of work done by the shear stress exerted by the fluctuating gas at the interface
$SUT = \frac{2\pi}{We} \int_0^A [\tilde{v}_1 (1 + \partial^2 / \partial z^2) \tilde{\eta}]_{r=1} dz$	Rate of work done by the surface tension
$SHB = \frac{2\pi}{Re} \int_0^A \tilde{\eta} \tilde{u}_1 (NU_2'' - U_1'')_{r=1} dz$	Rate of work done by the shear stress associated with the basic flow distortion
$NE = 2\pi \int_0^A \partial \tilde{\eta} / \partial z (\tilde{u}_1 \Gamma_{zz})_{r=1} dz$	Rate of work done by the unrelaxed axial elastic stress with the interface fluctuation
$DIS = - \iiint \tilde{T}_s : \nabla \tilde{V}_1 dV$	Rate of work contributed by the solvent viscous dissipation
$DIP = - \iiint \tilde{T}_p : \nabla \tilde{V}_1 dV$	Rate of work contributed by the elastic stress

Table 4. Physical interpretation of terms from the energy analysis.

appropriate to consider the relative rate of change of energy, i.e. dividing each energy term in (3.4) by the disturbance kinetic energy of the system, e.g.

$$\overline{KE} = \frac{KE}{DK}, \quad \overline{REY} = \frac{REY}{DK}, \quad \overline{PRG} = \frac{PRG}{DK}, \quad \text{etc.}, \quad (3.5a-c)$$

with the disturbance kinetic energy

$$DK = \iiint_{\substack{0 \leq z \leq A \\ 0 \leq r \leq 1}} \tilde{V}_1 \cdot \tilde{V}_1 / 2 dV. \quad (3.6)$$

As pointed out by Ye *et al.* (2016), the dimensionless relative rate of change of the disturbance kinetic energy is equal to the growth rate of the disturbance. Therefore, the relative energy terms quantitatively represent the contribution of each physical factor (surface tension, elastic tension, viscous dissipation, etc.) to the temporal growth rate. In the following, the relative rate of change of energy instead of the rate of change of energy will be adopted, and the superscript bar for each term in (3.5a-c) will be dropped for simplicity. In addition, it is easy to verify that when the hyperbolic-tangent function is used as the basic-velocity profile, the SHB term is actually equal to zero due to $U_1''(1) = U_2''(1) = 0$.

4. Results and discussion

4.1. Influence of fluid elasticity on jet instability

In this section, we discuss the influence of fluid elasticity on jet instability based on the variations of the growth rate s of disturbances with $s = kc_i$. In calculations, we choose the typical parameters as the reference state: $Re = 100$, $We = 3$, $X = 0.9$, $Q = 0.0013$, $N = 0.018$, $U_s = 1.2$ and $K = 0.9$. These dimensionless parameters are fixed to the reference values in the following discussion unless they are specifically stated.

Figure 3 illustrates the variations in the growth rate s with the dimensionless axial wavenumber k , for different parameters X and El but with the same value of $(1 - X)El$. It can be found that, for a dilute polymer solution ($X > 0.7$), there is no significant difference in the unstable growth rate curve under the same combination $(1 - X)El$. The present study is confined to considering the jet instability of a dilute polymer solution, so that one can investigate the influence of fluid elasticity on the jet instability by only changing El with a fixed X .

In figure 4, we explore the variations of the growth rate s for different El . As El is increased from 0 to 0.01, the growth rate of the disturbance shows a slight increase (figure 4b). As El is increased further, the growth rate shows a rapid decline. This indicates that the elasticity of the fluid plays a dual role in the analysis of jet stability: a viscoelastic jet composed of weakly elastic fluids exhibits more rapid growth of axisymmetric disturbances than a Newtonian one, while for viscoelastic jets with more pronounced elastic properties, the growth of axisymmetric disturbances is significantly suppressed. This feature is consistent with the experimental evidence for a laminar capillary jet of a viscoelastic fluid (Goldin *et al.* 1969), and has not been reported in the existing theoretical analyses, to the best of our knowledge. We believe that the above behaviour is universal in the viscoelastic jet instability, and it is essentially related to the nonlinear constitutive relation of viscoelastic fluids and non-uniform basic velocity.

It is noticed that, for a uniform basic-velocity profiles, the elastic stress tensor $\mathbf{\Gamma} = 0$. Thus, all nonlinear terms in the rheological constitutive equations are eliminated after linearization, giving the same results as those obtained using the Jeffreys model. The instability analysis was thus regarded to be independent of the form of the constitutive equations (Goldin *et al.* 1969; Ruo *et al.* 2011). However, when a non-uniform basic velocity is considered in the base-state solutions, as described in § 2.2, the nonlinear viscoelastic impacts will be preserved in the stability analysis. On the one hand, the non-uniform basic velocity induces a non-zero elastic stress tensor $\mathbf{\Gamma}$, including the unrelaxed axial elastic tension Γ_{zz} , based on the nonlinear constitutive equation. On the other hand, a coupling term between the elastic stress tensor and the perturbation velocity, i.e. $\langle \mathbf{\Gamma}, \tilde{\mathbf{V}}_1 \rangle$ in (2.19), is derived from the linearization of the constitutive equation, which reflects the nonlinear characteristics of the constitutive equation to some extent. Strictly speaking, the term $\langle \tilde{\mathbf{T}}_p, U_1 \rangle$ in (2.19) is also from the linearization of the nonlinear part of the constitutive equation. However, its impact on the jet instability is small relative to the term $\langle \mathbf{\Gamma}, \tilde{\mathbf{V}}_1 \rangle$ (see figure 8 for case B where the influence of $\langle \mathbf{\Gamma}, \tilde{\mathbf{V}}_1 \rangle$ is removed and the DIP including the contribution of $\langle \tilde{\mathbf{T}}_p, U_1 \rangle$ is negligibly small). Therefore, the influence of nonlinear elasticity can be predicted through the coupling term $\langle \mathbf{\Gamma}, \tilde{\mathbf{V}}_1 \rangle$.

Figure 5 shows the relative contribution of various factors in the rate of change of disturbance kinetic energy vs the wavenumber for different El . For small El , the effects of surface tension (represented by SUT) and external gas shear and pressure (represented by SHG and PRG) are significant factors on the instability in the long-wave and short-wave regions, respectively (see figure 5a). With the increase of El , the influence of fluid

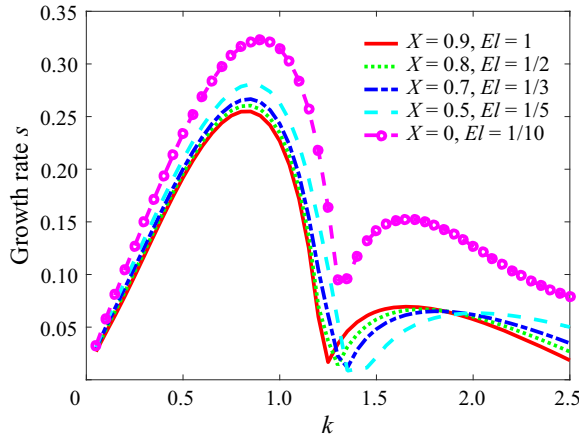


Figure 3. Variations of the growth rate s with the dimensionless axial wavenumber k for different parameters X and El but with the same combination $(1 - X)El = 0.1$.

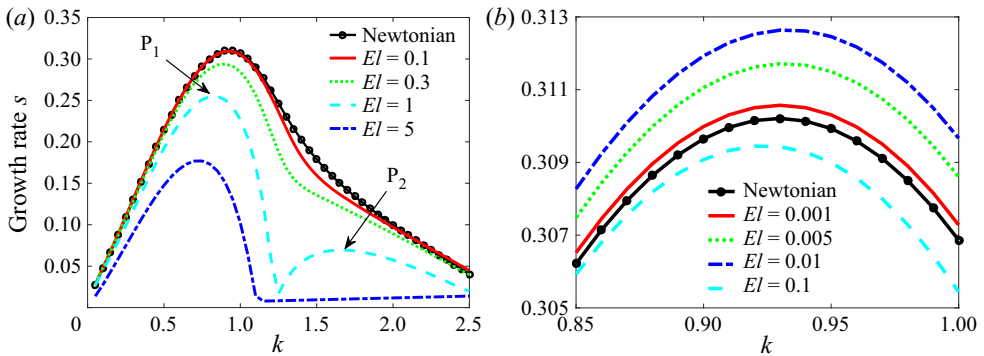


Figure 4. Variations of the growth rate s with the dimensionless axial wavenumber k for different El : (a) $El = 0.1, 0.3, 1, 5$; (b) $El = 0.001, 0.005, 0.01, 0.1$. Note that (b) shows the enlarged region near the maximum growth rate. Obviously, there are two peaks (denoted by P_1 and P_2) for $El = 1$ in (a), indicating that two different instability modes may appear at the corresponding locations (wavenumbers). With the help of the energy budget method, it can be further confirmed that P_1 corresponds to elastic instability while P_2 corresponds to shear instability (refer to the last paragraph in § 4.1 for detailed descriptions of the instabilities).

elasticity (represented by NE and DIP) begins to increase gradually and finally becomes dominant (figures 5(b) and 5(c)). It is notable that NE and DIP make completely opposite contributions to the rate of change of disturbance energy: NE tends to amplify the disturbance kinetic energy, thereby promoting the instability; on the contrary, DIP tends to reduce the kinetic energy of disturbance, thereby suppressing the jet instability. Note that NE is related to the unrelaxed elastic tension whereas DIP includes the influence of the coupling term $(\mathbf{T}, \tilde{V}_1)$ in the constitutive equation. The combined effect of NE and DIP is shown in figure 5(d). The NE is dominant for $Wi < O(1)$, while DIP is dominant for $Wi > O(1)$. In summary, the influence of fluid elasticity on the jet instability is mainly controlled by the magnitudes of NE and DIP, and the competition between NE and DIP is determined by Wi .

As is well known, Wi quantifies the nonlinear response of the viscoelastic fluid (Galindo-Rosales *et al.* 2014; Ding & Jian 2021) (note that the factor Wi appears in front

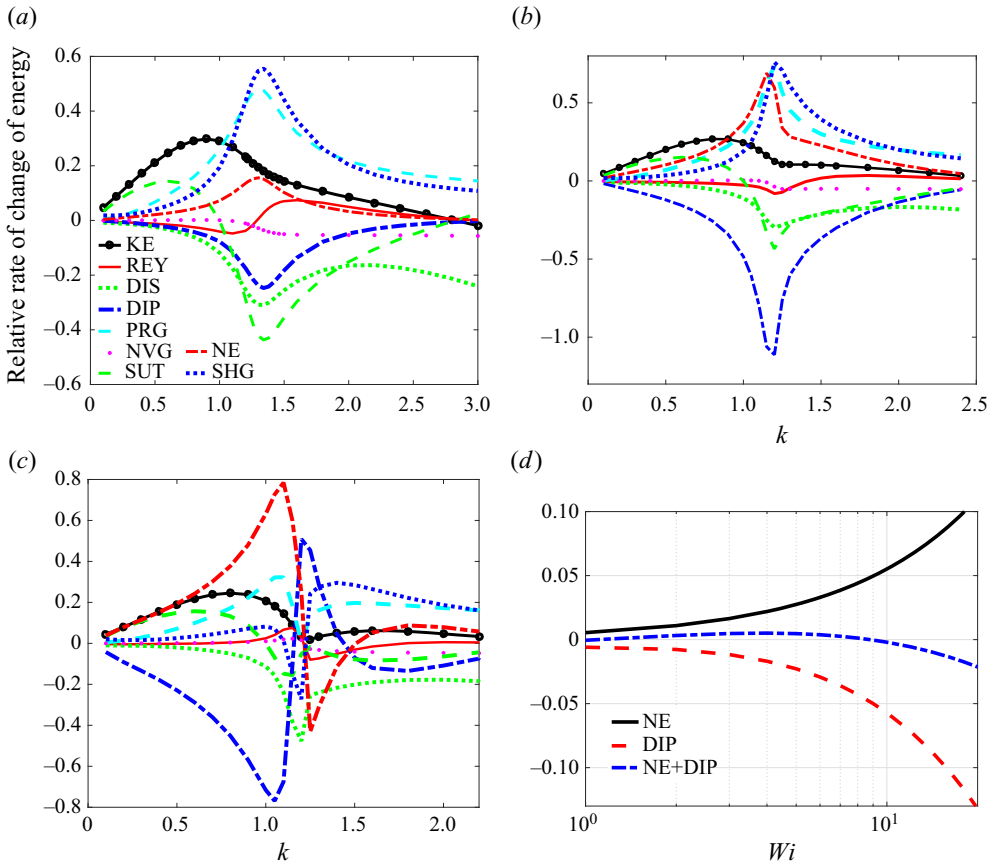


Figure 5. Energy budget, using the relative rate of change of energy, vs the wavenumber for (a) $El = 0.1$, (b) $El = 0.5$ and (c) $El = 1$. Here, the meanings of the letters can be found in table 4. Note that, in (c), the abrupt changes near $k \approx 1.2$ may be due to the increase in the calculation error caused by the mode transition (see figure 4(a) for $El = 1$). (d) Comparison of the relative sizes of NE and DIP with the change of Wi . When $Wi < O(1)$, $|NE| > |DIP|$, while for $Wi > O(1)$, $|NE| < |DIP|$.

of the nonlinear terms of the constitutive equation (2.3)). Thus for $Wi < O(1)$, the linear terms of the constitutive equation dominate the nonlinear parts, and the magnitude of NE exceeds the one of DIP (as shown in figure 5d), so that the perturbation growth rate shows an increasing trend. While for $Wi > O(1)$, a strong nonlinear effect is stimulated, and the magnitude of DIP exceeds that of NE, so that the perturbation growth rate shows a downward trend. This is consistent with the change of disturbance growth rate shown in figure 4(b), where the critical $El \sim 0.01$ corresponds to $Wi \sim 1$.

Figure 6 further shows the variations of the maximum perturbation growth rate with Wi . It is found that, when $Wi < O(1)$, the viscoelastic jet is less stable than its Newtonian counterpart, since the nonlinear viscoelastic effect is insignificant and the unrelaxed tension promotes the instability of the jet. While in the range of $Wi > O(1)$, the nonlinear viscoelastic effect greatly suppresses the maximum growth rate, which makes the viscoelastic jet more stable than the Newtonian one.

In order to demonstrate the influences of the nonlinear elasticity and the unrelaxed elastic tension more clearly, we consider two specific cases: (i) using a linear viscoelastic model, i.e. the Jeffreys model – case A, in which the unrelaxed axial elastic tension Γ_{zz}

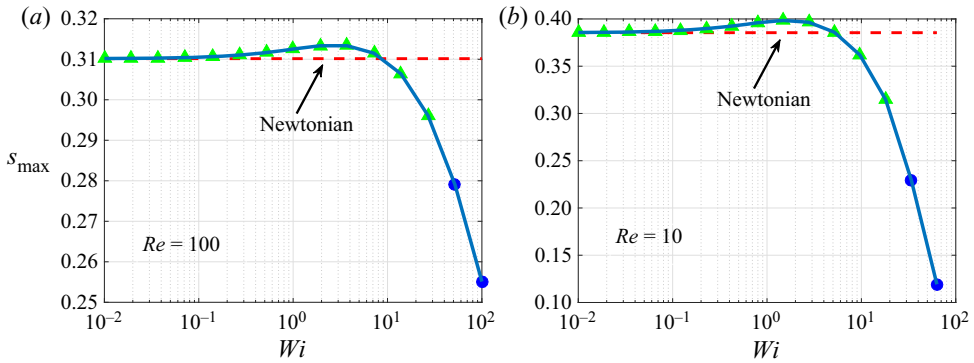


Figure 6. Variations of the maximum growth rate s_{\max} ($s_{\max} = \max_k\{s\}$) with the Weissenberg number Wi for (a) $Re = 100$ and (b) $Re = 10$, where the green triangles (\blacktriangle , green) represent the shear instability (SI) modes and the blue circles (\bullet , blue) represent the elastic instability (EI) modes (the detailed definitions of these instability modes are given in the penultimate paragraph in § 4.1). Here, the Newtonian maximum growth rate is also shown (dashed line) for reference. It is notable that the forms of the variations of the growth rate for different Re are unified by means of Wi . Specifically, the growth rate of disturbance increases slightly with $Wi < O(1)$, while it decreases rapidly with $Wi > O(1)$.

and the coupling term $\langle \mathbf{T}, \tilde{\mathbf{V}}_1 \rangle$ does not appear in spite of the non-uniform basic velocity considered; (ii) using the Oldroyd-B model with the coupling term $\langle \mathbf{T}, \tilde{\mathbf{V}}_1 \rangle$ removed in (2.19) – case B. In case A, the influences of both the unrelaxed elastic tension and nonlinear elasticity are eliminated at the same time. Compared with the full Oldroyd-B model, case B is able to show the effect of Γ_{zz} alone without being limited by the nonlinear factors.

The variations of the growth rate s of disturbance for cases A and B are shown in figures 7(a) and 7(b), respectively. As El is increased from 0 to 0.1 in case A, the growth rate shows a slight increase, and when El continues to increase, the growth rate reaches saturation and hardly changes. The slight promotion effect of linear viscoelasticity on the growth rate is consistent with the above analysis. However, for case B, the growth rate increases continuously with El due to the presence of the unrelaxed elastic tension. In other words, the unrelaxed elastic tension further promotes the increase in the growth rate of the disturbance. Compared with the full Oldroyd-B model, the downward trend of the growth rate does not appear due to the lack of the nonlinear elasticity. From the perspective of energy budget analysis, as shown in figure 8, NE becomes dominant in the jet instability and promotes the increase in the growth rate with the increase of El for case B. It is notable that the contribution of the DIP term related to the nonlinear elasticity effect on the growth rate of the disturbance is almost negligible in case B. Comparing with the full Oldroyd-B model, this illustrates the significance of the coupling term $\langle \mathbf{T}, \tilde{\mathbf{V}}_1 \rangle$ in the nonlinear elastic behaviour of the jet.

In the linear and nonlinear regimes of fluid elasticity, the structure of the spectrum is also different, which is discussed in detail in Appendix B. In the linear regime (i.e. $Wi < O(1)$), the ring structure in the viscoelastic spectrum is prominent, whereas in the nonlinear regime ($Wi > O(1)$), the ring collapses into the continuous spectra in an irregular manner. In addition, by tracking its trajectory, we find the most unstable eigenvalue falls into the continuous spectrum balloon when $(1 - X)El \sim 1$, which leads to a sharp deterioration in the accuracy and convergence for resolving the most unstable eigenvalue.

Based on the energy analysis, three different types of instability mechanism can be identified in the present work. First, similar to the case of Newtonian jets, the predominance of the SUT term characterizes the instability caused by surface tension,

Instability of viscoelastic jet in co-flowing gas stream

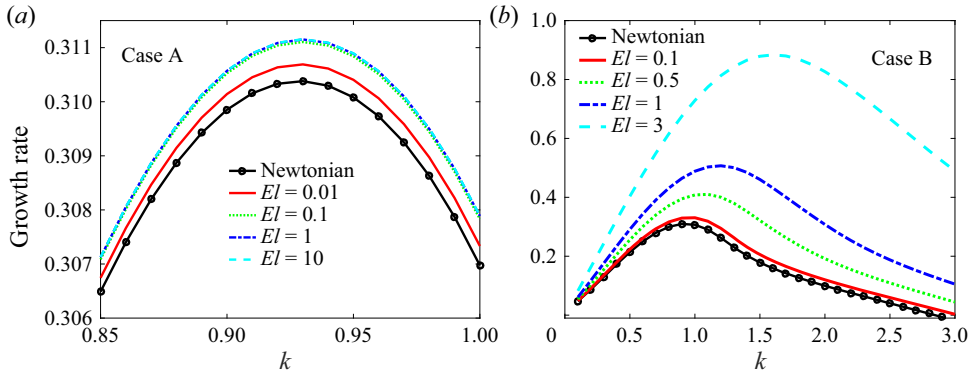


Figure 7. Variations of the growth rate s of (a) the Jeffreys model – case A and (b) the Oldroyd-B model without the coupling term (Γ, \tilde{V}_1) – case B, vs the wavenumber k for different El . Note that (a) shows the enlarged region near the maximum growth rate, like figure 4(b). It can be observed that, when $El > 0.1$, the growth rate in case A hardly changes with the increase of El , whereas the growth rate in case B continues to increase with El .

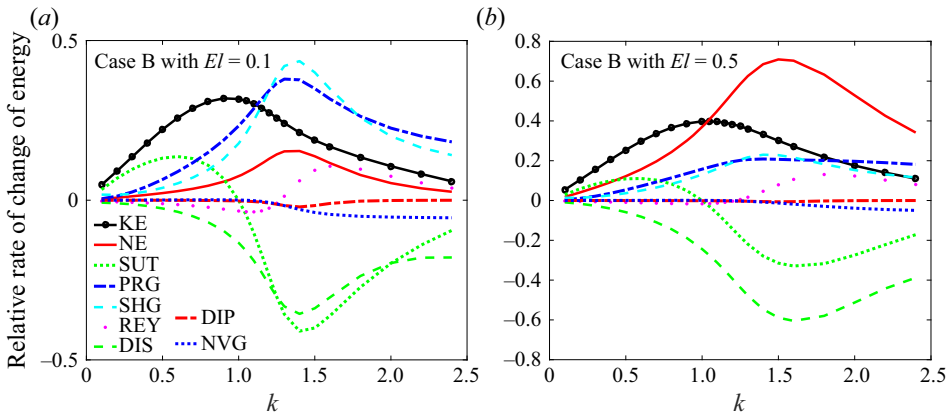


Figure 8. Energy budget, using the relative rate of change of energy, vs the wavenumber for case B, where (a) $El = 0.1$ and (b) $El = 0.5$.

which can be called the capillary instability (abbreviated as CI), while the predominance of SHG or PRG corresponds to the instability caused by external gas shear and pressure, called the shear instability (abbreviated as SI). In addition, a new instability mechanism can be identified, where the elastic effect (i.e. NE) plays a dominant role in the instability of a viscoelastic jet, and this instability is called the elastic instability (abbreviated as EI). The previous analysis of figures 4–8 is helpful to understand the mechanism and features of EI. Importantly, the nonlinear elastic effect in the EI regime plays a stabilizing role in the jet.

With the help of energy budget analysis and identification of instability modes, we can explore the instability mechanisms in figure 4(a), and determine the instability modes at the peaks (denoted by P_1 and P_2). For small El (e.g. $El = 0.1$), the instability of a jet is attributed to SI since the contributions of SHG and PRG to the instability are dominant at the most dangerous disturbance wavenumber $k \approx 1$ (figure 5a). As El increases to 1, the elastic effect becomes enhanced, and the instability of the jet belongs to EI in the long-wave region, while SI is still the main instability mode

in the short-wave region (figure 5c). Comparing the maximum growth rates in the long-wave and short-wave regions, it can be seen that the maximum growth rate in the long-wave region is significantly larger (figure 4a), and thus the dominant mechanism of instability for $El = 1$ in figure 4(a) is attributed to EI. In this paper, we mainly focus on the instability corresponding to the maximum growth rate over the entire wavelength range.

4.2. General features of instability modes

To gain more insight into the instability, we depict the variations in the maximum growth rate over the entire wavelength range, i.e. $s_{\max} = \max_k\{s\}$, and the corresponding phase speed, $c_{r,\max}$, with the relevant parameters in figure 9. Note that the unstable eigenvalues are usually located on the I_1 branch (figure 13), but this does not mean that the external gas does not contribute to the instability. In fact, we have known from the analysis in § 4.1 that the effect of external gas is the source of SI. As El increases, the transition of the instability mode from CI (or SI) to EI occurs (see figure 9a), as expected. In the EI regime, the growth rate decreases approximately linearly with El . In addition, the transitions from SI (or EI) to CI and from CI to SI occur with the increase of We^{-1} and K , respectively (figures 9(c) and 9(e)). The growth rates in the CI and SI regimes increase approximately linearly with We^{-1} and K , respectively. The phase diagrams on the mode transitions in different parameter spaces will be given in § 4.3.

With increasing El , the phase speed c_r in the EI regime decreases and tends to the basic velocity at the centre of the internal fluid (i.e. $c_r \rightarrow 1$ in figure 9b), so the EI mode can be also called the centre mode. This feature is analogous to the centre mode instability in viscoelastic Poiseuille flow (Garg *et al.* 2018; Khalid *et al.* 2021). In figure 9(d), with the decrease of We , the phase speed in the CI regime decreases (suppressed), and then gradually tends to a constant value. However, the phase speed in the CI regime is always above the average velocity of the jet, and stays near the velocity U_s at the jet interface, so the CI mode can be also called the interface mode. In figure 9(f), it can be observed that, as K increases, the phase speed in the SI regime increases (promoted), which tends to the velocity in the shear layer of the external gas, so the SI mode can be called the shear mode. The above features on the growth rate and phase speed under the three instability modes are summarized in table 5.

The velocity and polymer stress eigenfunctions corresponding to the unstable eigenvalues are shown in figure 10. It can be found that, as El increases, the axial velocity eigenfunctions gradually approach the centre of the jet (i.e. $r = 0$) in the EI regime, which is consistent with the behaviour of the eigenvalues, although the eigenfunctions are not localized near the centreline. In contrast, the axial disturbance velocity fields are almost uniform, spreading across the cross-section of the liquid jet for the parameters considered in the CI regime (corresponding to small We ; see figure 10c). The amplitude of the axial velocity eigenfunction in figure 10(d) is significantly larger near the interface (i.e. $r \approx 1$) than that at the centre due to the dominance of the shearing effect in the SI regime. In addition, the \hat{v}_{zz} eigenfunction shows a sharp peak for large El near the boundary layer of the liquid jet, in which a large velocity gradient appears for the basic velocity.

4.3. Transitions of instability modes in parameter space

In the previous section, we have analysed the characteristics of the three instability modes in detail. In this section, we focus on the transition boundaries between different modes (i.e. CI/SI, CI/EI and SI/EI) in parameter space.

Instability of viscoelastic jet in co-flowing gas stream

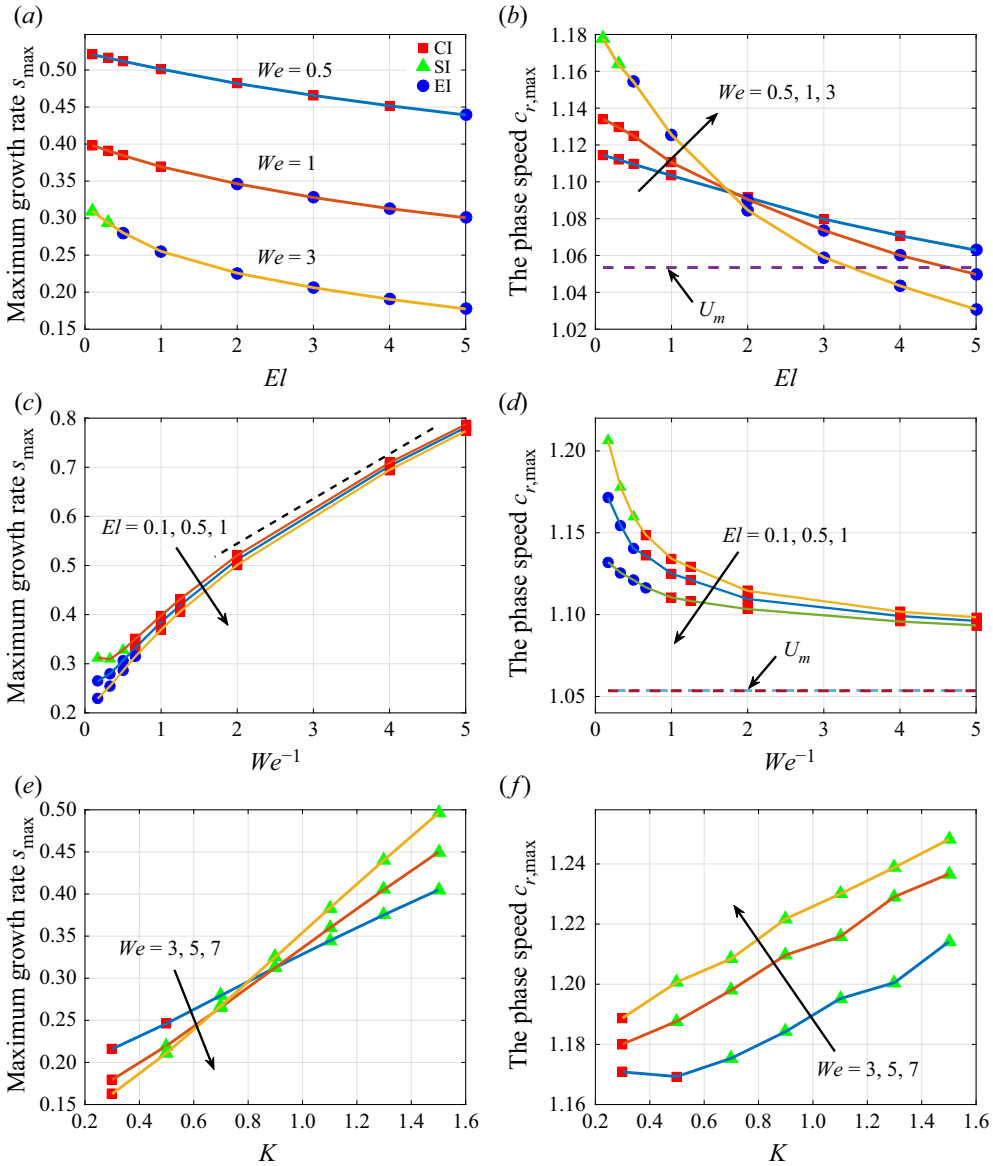


Figure 9. Variations of the maximum growth rate s_{\max} and the corresponding phase speed $c_{r,\max}$ of disturbances with (a,b) El , (c,d) We^{-1} and (e,f) K for a fixed $El = 0.01$. Here, $Re = 100$, $Q = 0.0013$, $N = 0.018$, $U_s = 1.2$. The red squares represent the CI modes, the green triangles represent the SI modes and the blue circles represent the EI modes. In (b,d), the dimensionless average velocity U_m of the jet at the basic state is shown for reference. The growth rate in the EI regime in (a) decreases approximately linearly with the increase of El , while the growth rates increase approximately linearly with the increase of We^{-1} and K in the CI and SI regimes of (c,e), respectively.

Figure 11(a) shows the transition between CI and SI on a $We-K$ plane for very small El ($El = 0.01$). As We or K increases, the transition of the instability mode from CI to EI occurs. The transition boundary of CI/SI is found to approximately satisfy the curve $l_1: KWe = c_1$, with the constant c_1 depending on Re (see table 7). As El increases, the EI mode appears, which has been known from the previous discussion. Figure 11(b) shows

Instability mode	Control parameter	Growth rate s	Phase speed c_r	Wavelength type
CI	$We \downarrow$	Promoted \uparrow	Suppressed \downarrow	Long-wave instability
SI	$K \uparrow$	Promoted \uparrow	Promoted \uparrow	Short-wave instability
EI	$El \uparrow$	Suppressed \downarrow	Suppressed \downarrow	Long-wave instability

Table 5. The features on the growth rate and phase speed for the instability modes CI, SI and EI.

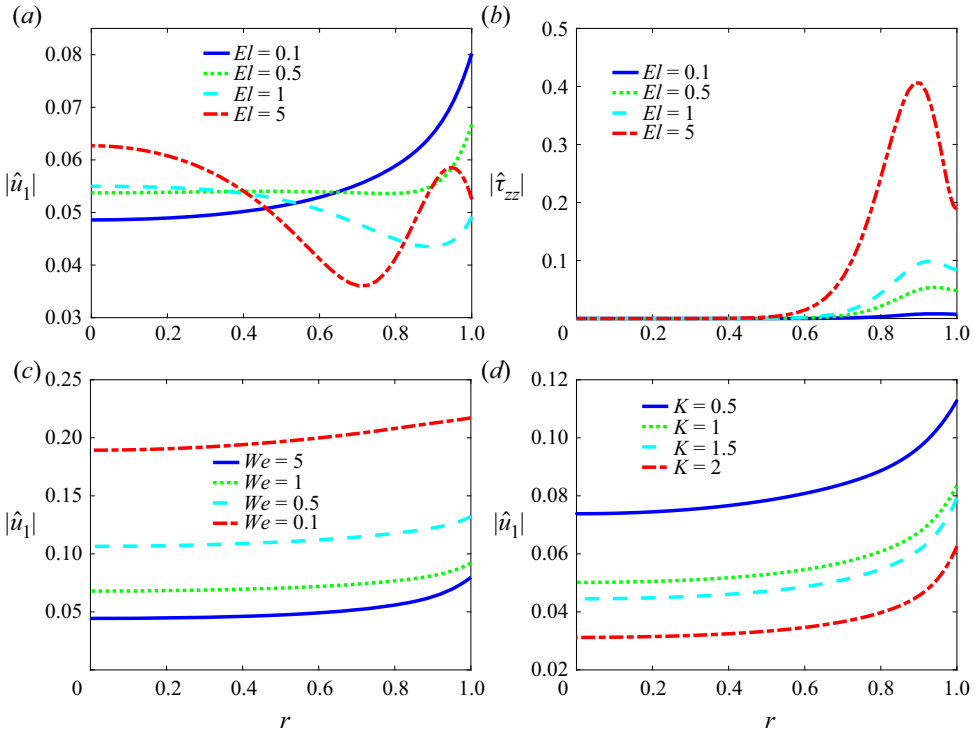


Figure 10. Profiles of the axial (a) velocity and (b) polymer stress of the disturbance corresponding to unstable eigenvalues at different El with $k = 0.8$, $X = 0.9$, $Re = 100$, $We = 3$, $U_s = 1.2$ and $K = 0.9$. (c,d) Show the profiles of the axial velocity of the disturbance at different We and K , respectively, with $El = 0.1$. Here, the moduli of the velocity and stress are calculated because they are complex variables. In (a) the axial velocity profiles for large El correspond to EI modes, while in (c) the velocity profiles for small We correspond to CI modes and in (d) the velocity profiles correspond to SI modes.

the transition between CI and EI on a El - K plane for small We ($We = 0.5$). Note that a large value of K means a large velocity gradient for the basic velocity of the jet (see (2.12)), thereby resulting in a large unrelaxed axial elastic tension Γ_{zz} , which makes the EI tend to dominate even at a small value of El . The transition boundary of CI/EI is found to approximately satisfy the curve $l_2: We^\gamma (1 - X)El K^\alpha = c_2$ with $\alpha = 3$ and $\gamma = 1.5$, where the constant c_2 depends on Re .

For certain parameter ranges (e.g. small El or We), only two instability modes and their transitions (e.g. CI/SI or CI/EI) can be observed (figures 11(a) and 11(b)). While, for large El or We , three instability modes and their transitions are usually observed. Figures 11(c) and 11(d) show the transition boundaries of CI/SI, CI/EI and SI/EI on a

Instability of viscoelastic jet in co-flowing gas stream

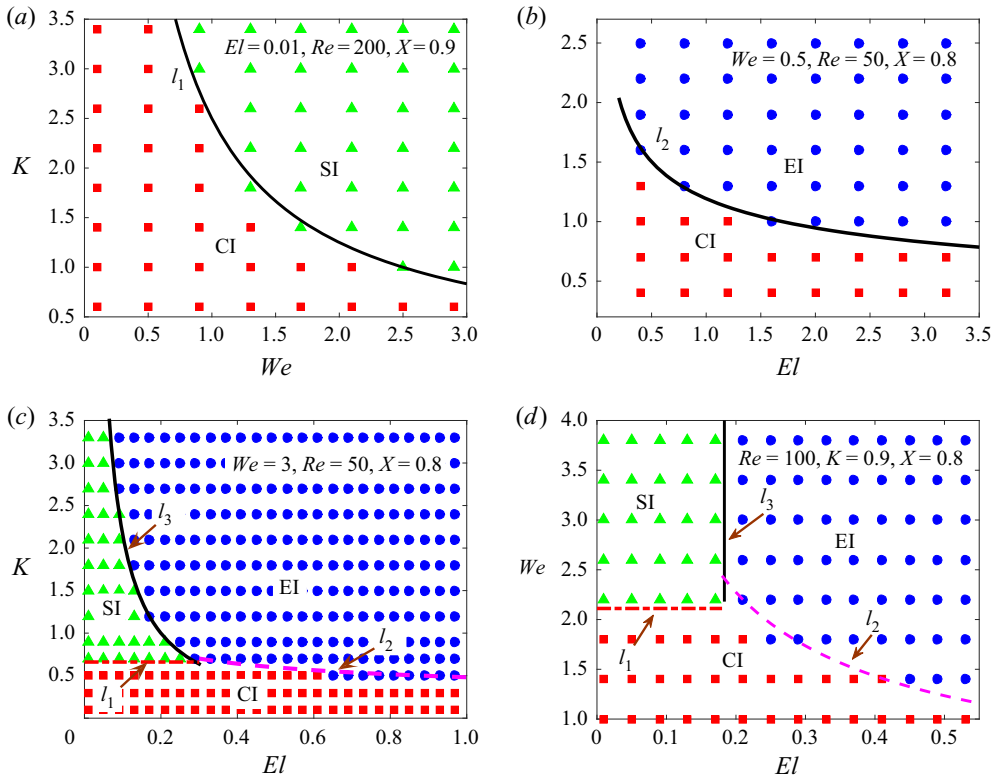


Figure 11. (a) Phase diagram of CI/SI mode on a We - K plane at $Re = 200$, $El = 0.01$ and $X = 0.9$. (b) Phase diagram of CI/EI mode on a El - K plane at $We = 0.5$, $Re = 50$ and $X = 0.8$. (c) Phase diagrams of CI/SI, CI/EI and SI/EI on a El - K plane at $We = 3$, $Re = 50$, $X = 0.8$. (d) Phase diagrams of CI/SI, CI/EI and SI/EI on a El - We plane at $Re = 100$, $K = 0.9$ and $X = 0.8$. The red squares (■, red) represent the CI mode, the green triangles (▲, green) represent the SI mode and the blue circles (●, blue) represent the EI mode. The transition boundary of CI/SI mode is close to the curve $l_1: KWe = c_1$; the transition boundary of CI/EI mode is close to the curve $l_2: We^\gamma(1-X)EK^\alpha = c_2$ with $\alpha = 3$ and $\gamma = 1.5$; while the transition boundary of SI/EI mode is close to the curve $l_3: (1-X)EK^\beta = c_3$ with $\beta = 1$. Here, the constants c_1 , c_2 and c_3 depend on Re , which are listed in table 7. Note that, in (c), the boundary curve l_1 of CI/SI is a horizontal line on a El - K plane for a fixed We . In (d) the boundary curves l_1 and l_3 of CI/SI and SI/EI are the horizontal and vertical lines, respectively, on a El - We plane for fixed K and X .

El - K or El - We plane, where the curves l_1 and l_2 are still valid at large We (e.g. $We = 3$) for the transition boundaries of CI/SI and CI/EI, respectively. Furthermore, the transition boundary of SI/EI is approximately given by the curve $l_3: (1-X)EK^\beta = c_3$ with $\beta = 1$. In all cases, the transition boundaries of CI/SI, CI/EI and SI/EI and the values of c_1 , c_2 and c_3 are summarized in tables 6 and 7, respectively. Note that the transition boundary of CI/SI is a straight line on the $El - K$ plane with a fixed We or on the El - We plane with a fixed K , and the transition boundary of SI/EI is a straight line on the El - We plane for a fixed K (figures 11(c) and 11(d)).

Figure 12 displays the variations of the transition boundaries of CI/SI, CI/EI and SI/EI with related parameters. From figure 12(a), it can be found that the boundary of CI/SI would shift up as Re increases, i.e. the CI region expands and the SI region shrinks, because the constant c_1 increases with the increase of Re . The boundary of CI/EI varies slightly with Re due to the weak dependence of c_2 on Re (figure 12(b)). In figure 12(c),

Mode transition	Boundary curve	Parameters
CI/SI	$l_1: KWe = c_1$	$\alpha = 3, \gamma = 1.5$ $\beta = 1$
CI/EI	$l_2: We^\gamma(1-X)EK^\alpha = c_2$	
SI/EI	$l_3: (1-X)EK^\beta = c_3$	

Table 6. The approximate transition boundaries between different modes (CI/SI, CI/EI and SI/EI) in the parameter space, where the constants c_1, c_2 and c_3 depend on Re and their values are provided in table 7.

Re	c_1	c_2	c_3
50	1.7	0.12	0.045
100	2.3	0.14	0.033
400	2.8	0.19	0.026

Table 7. The values of c_1, c_2 and c_3 are provided for different Re .

the boundary of CI/EI would shift down as We increases, i.e. the CI region would shrink, which is consistent with the fact that a large We characterizes relatively small surface tension. While for large X , i.e. a large solvent component, the influence of fluid elasticity is weakened, resulting in the contraction of the EI region (figures 12(d) and 12(f)). In addition, since the constant c_3 decreases with the increase of Re (see table 7), the boundary of SI/EI would shift down as Re increases (figure 12e).

5. Conclusions

The present study provides a comprehensive account of the linear instability of viscoelastic jets, where the importance of a non-uniform basic velocity is clarified for the first time. Especially, a new unrelaxed axial elastic tension is derived based on a non-uniform basic velocity, which is significantly different from Goren & Gottlieb’s theory. The unrelaxed elastic tension depends on the velocity gradient, elasticity number and solvent viscosity ratio. To carry out the linear stability analysis, the base state is subjected to small amplitude axisymmetric disturbances. After neglecting high-order terms, the linearized governing equations together with the linearized boundary conditions can be derived, which constitute a generalized eigenvalue problem. Despite its complexity, we successfully solve this problem by employing a spectral collocation method. Furthermore, to better understand the mechanism of jet instability, an analysis of the energy budget of the destabilization process is performed over a control volume of one disturbance wavelength.

Our results show that the elasticity of fluid plays a dual role in the analysis of jet stability: a viscoelastic jet composed of weakly elastic fluids exhibits more rapid growth of axisymmetric disturbances than a Newtonian one, while for viscoelastic jets with more pronounced elastic properties, the growth of axisymmetric disturbances is significantly suppressed. This feature is essentially related to the nonlinear constitutive relation of viscoelastic fluids and the non-uniform basic velocity. When $Wi < O(1)$, the linear terms of the constitutive equation dominate the nonlinear parts, and the linear elasticity of fluids leads to an increase in the growth rate of disturbance. While when $Wi > O(1)$, a strong nonlinear effect is stimulated by the coupling term $\langle \boldsymbol{\Gamma}, \tilde{\mathbf{V}}_1 \rangle$ between the elastic stress tensor and perturbation velocity, where the non-zero elastic stress tensor is induced by non-uniform basic velocity. The nonlinear elasticity of fluids has a significant inhibitory

Instability of viscoelastic jet in co-flowing gas stream

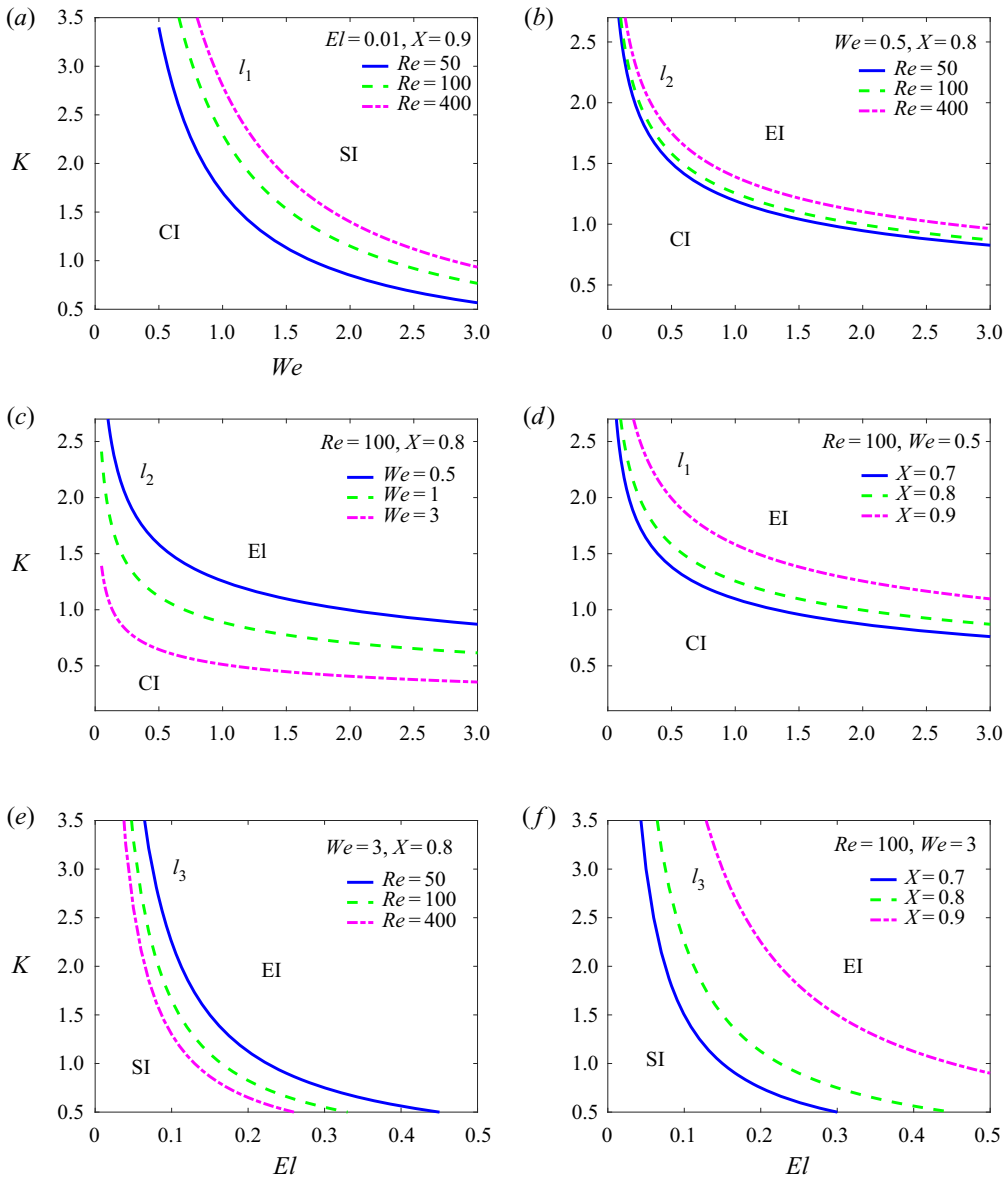


Figure 12. Variations of the transition boundaries of CI/SI, CI/EI and SI/EI with related parameters, where (a) $El = 0.01$ and $X = 0.9$ with $Re = 50, 100, 400$; (b) $We = 0.5$ and $X = 0.8$ with $Re = 50, 100, 400$; (c) $Re = 100$ and $X = 0.8$ with $We = 0.5, 1, 3$; (d) $Re = 100$ and $We = 0.5$ with $X = 0.7, 0.8, 0.9$; (e) $We = 3$ and $X = 0.8$ with $Re = 50, 100, 400$; (f) $Re = 100$ and $We = 3$ with $X = 0.7, 0.8, 0.9$.

effect on the disturbance growth rate. These assertions are supported by the results of the energy analysis, and are further verified by considering two specific cases: (i) using a linear viscoelastic model, i.e. the Jeffreys model – case A; (ii) using the nonlinear Oldroyd-B model with the coupling term $\langle \Gamma, \tilde{V}_1 \rangle$ removed – case B

Based on the energy budget analysis, three different instability mechanisms can be identified, which correspond to three instability modes, i.e. the capillary instability (CI), shear instability (SI) and elastic instability (EI) modes. For the CI mode, the surface

tension is dominant in the jet instability; for the SI mode, the shear and pressure of external gas are dominant in the jet instability; and for the EI mode, the elastic tension plays a dominant role in the jet instability. The general features of these instability modes are explored. It is found that both the growth rate and phase speed of the disturbances are promoted in the SI regime, while they are both suppressed in the EI regime. In contrast, the growth rate in the CI regime is promoted, whereas the phase speed in the CI regime is suppressed. Furthermore, in the EI regime, the phase speed tends to the basic velocity at the centre of the jet and the corresponding velocity eigenfunction also gradually approaches the centre as El increases, but the eigenfunction is not localized near the centreline. Although the phase speed in the CI regime is also decreasing, it is always above the average velocity of the jet, which means that it does not tend to the basic velocity at the centre, and the corresponding velocity eigenfunction is almost uniform, spreading across the cross-section of the liquid jet. In contrast, the phase speed in the SI regime is increasing, and tends to the velocity in the shear layer of the external gas, and the amplitude of the corresponding velocity eigenfunction is significantly larger near the interface due to the dominance of the shearing effect in the SI regime. In addition, the eigenfunction for the axial elastic stress shows a sharp peak near the boundary layer of the liquid jet, where a large velocity gradient appears in the basic velocity.

Finally, we investigate the transitions of instability modes in parameter spaces and provide the transition boundaries between different modes (i.e. CI/SI, CI/EI and SI/EI). This study provides guidance for understanding the mechanism of instability of viscoelastic jets in a co-flowing gas stream and the transition criterion of instability modes.

Funding

This work was supported by the National Natural Science Foundation of China (Z.D., grant number 11902165), (T.S., grant numbers 12027801, 11621202), (K.M., grant number 11902318), (Y.J., grant number 11772162); the Youth Innovation Promotion Association CAS (T.S., grant number 2018491); and the Natural Science Foundation of Inner Mongolia Autonomous Region of China (Z.D., grant number 2019BS01004).

Declaration of interests

The authors report no conflict of interest.

Author ORCIDs.

- ① Zhaodong Ding <https://orcid.org/0000-0003-3560-9003>;
- ① Kai Mu <https://orcid.org/0000-0002-4743-2332>;
- ① Ting Si <https://orcid.org/0000-0001-9071-8646>;
- ① Yongjun Jian <https://orcid.org/0000-0003-0263-8422>.

Appendix A. The linearized governing equations and boundary conditions

Substituting (2.22) into the governing equations (2.16)–(2.21), we obtain the following set of linearized governing equations:

$$\hat{v}'_1 + \frac{1}{r} \hat{v}_1 + ik\hat{u}_1 = 0, \tag{A1}$$

$$ik(U_1 - c) \hat{v}_1 = -\hat{p}'_1 + \frac{X}{Re} \left[\hat{v}''_1 + \frac{1}{r} \hat{v}'_1 - \frac{1}{r^2} \hat{v}_1 - k^2 \hat{v}_1 \right] + \hat{\tau}'_{rr} + \frac{1}{r} \hat{\tau}_{rr} + ik\hat{\tau}_{rz} - \frac{1}{r} \hat{\tau}_{\theta\theta}, \tag{A2}$$

Instability of viscoelastic jet in co-flowing gas stream

$$ik(U_1 - c)\hat{u}_1 = -U'_1\hat{v}_1 - ik\hat{p}_1 + \frac{X}{Re} \left[\hat{u}'_1 + \frac{1}{r}\hat{u}'_1 - k^2\hat{u}_1 \right] + \hat{\tau}'_{rz} + \frac{1}{r}\hat{\tau}_{rz} + ik\hat{\tau}_{zz}, \quad (A3)$$

$$[1 + ikWi(U_1 - c)]\hat{\tau}_{rr} = 2ik(1 - X)ElU'_1\hat{v}_1 + 2\frac{1 - X}{Re}\hat{v}'_1, \quad (A4)$$

$$[1 + ikWi(U_1 - c)]\hat{\tau}_{rz} + Wi \left[-U'_1\hat{\tau}_{rr} + \frac{1 - X}{Re}U''_1\hat{v}_1 - 2ik(1 - X)El(U'_1)^2\hat{v}_1 - \frac{1 - X}{Re}U'_1(\hat{v}'_1 + ik\hat{u}_1) \right] = \frac{1 - X}{Re}(\hat{u}'_1 + ik\hat{v}_1), \quad (A5)$$

$$[1 + ikWi(U_1 - c)]\hat{\tau}_{\theta\theta} = \frac{2(1 - X)\hat{v}_1}{Re r}, \quad (A6)$$

$$[1 + ikWi(U_1 - c)]\hat{\tau}_{zz} - 2WiU'_1 \left[\hat{\tau}_{rz} - 2(1 - X)ElU''_1\hat{v}_1 + 2ik(1 - X)ElU'_1\hat{u}_1 + \frac{1 - X}{Re}\hat{u}'_1 \right] = \frac{2(1 - X)}{Re}ik\hat{u}_1, \quad (A7)$$

$$\hat{v}'_2 + \frac{1}{r}\hat{v}_2 + ik\hat{u}_2 = 0, \quad (A8)$$

$$ik(U_2 - c)\hat{v}_2 = -\frac{1}{Q}\hat{p}'_2 + \frac{1}{Re} \frac{N}{Q} \left[\hat{v}''_2 + \frac{1}{r}\hat{v}'_2 - \frac{1}{r^2}\hat{v}_2 - k^2\hat{v}_2 \right], \quad (A9)$$

$$ik(U_2 - c)\hat{u}_2 = -U'_2\hat{v}_2 - \frac{ik}{Q}\hat{p}_2 + \frac{1}{Re} \frac{N}{Q} \left[\hat{u}''_2 + \frac{1}{r}\hat{u}'_2 - k^2\hat{u}_2 \right]. \quad (A10)$$

Here, the prime denotes the derivative with respect to r .

For the boundary conditions, the velocity and pressure at the symmetry axis satisfy the consistency conditions

$$\hat{v}_1 = \hat{u}'_1 = \hat{p}'_1 = 0, \quad \text{at } r = 0. \quad (A11)$$

At the liquid–gas interface, the continuity of velocity, the kinematic boundary condition and the balance of the normal and tangential stresses are satisfied, i.e.

$$\hat{v}_1 = \hat{v}_2, \quad (A12)$$

$$\hat{u}_1 - \hat{u}_2 + (U'_1 - U'_2)\hat{\eta} = 0, \quad (A13)$$

$$ik(U_1 - c)\hat{\eta} = \hat{v}_1, \quad (A14)$$

$$\hat{p}_1 - \hat{p}_2 + \frac{2N}{Re}\hat{v}'_2 - \frac{2X}{Re}\hat{v}'_1 - \hat{\tau}_{rr} = -\frac{1}{We}(1 - k^2)\hat{\eta}, \quad (A15)$$

$$\frac{N}{Re}U''_2\hat{\eta} + \frac{N}{Re}(\hat{u}'_2 + ik\hat{v}_2) = \frac{1}{Re}U''_1\hat{\eta} + \frac{X}{Re}(\hat{u}'_1 + ik\hat{v}_1) - 2ik(1 - X)El(U'_1)^2\hat{\eta} + \hat{\tau}_{rz}, \quad (A16)$$

at $r = 1$.

At the outside boundary,

$$\hat{v}_2 = \hat{u}'_2 = \hat{p}'_2 = 0, \quad \text{at } r = a, \quad (A17)$$

with $a = R_2/R_1$.

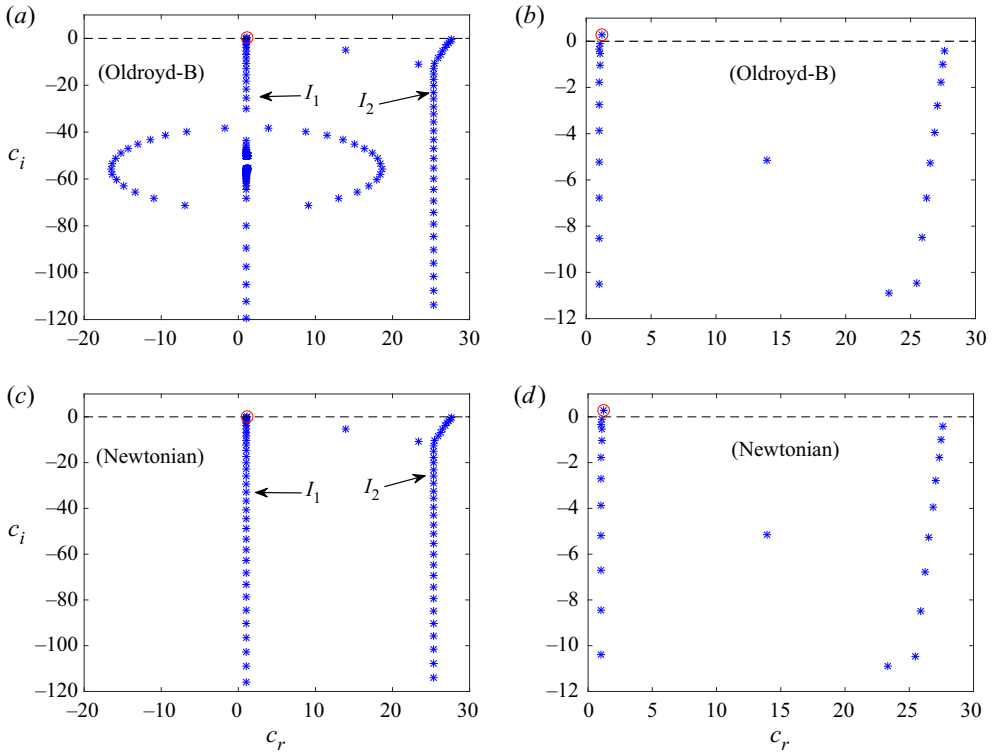


Figure 13. Eigenspectra of the jet for (a) Oldroyd-B ($El = 2 \times 10^{-4}$ and $X = 0.9$) and (c) Newtonian fluids, at $k = 1$, $Re = 100$, $We = 3$, $Q = 0.0013$, $N = 0.018$, $U_s = 1.2$, $K = 0.9$; (b,d) show the enlarged regions near the unstable eigenvalue (marked by the red circle) in (a,c), respectively. In order to ensure the accuracy, the eigenspectra are obtained using $N_1 = 120$ and $N_2 = 100$. For both Newtonian and viscoelastic jets, the structure of spectrum is composed of two separate parts (denoted by I_1 and I_2): the I_1 branch corresponds to the internal fluid (liquid); while the I_2 branch corresponds to the external gas. Obviously, the unstable eigenvalues are usually located on the I_1 branch. In contrast to the Newtonian case, a ring structure appears on the I_1 branch in viscoelastic spectra. However, for small El , the eigenspectra of the Oldroyd-B and Newtonian jets near the unstable eigenvalue are similar (see (b,d)).

Appendix B. Eigenspectrum of viscoelastic jets

Using the numerical method in § 2.4, the viscoelastic jet spectrum can be obtained. Figure 13 shows the eigenspectrum for an Oldroyd-B jet, where the spectrum for a Newtonian jet with the same configuration is also shown for reference. It can be found that the structure of spectrum is composed of two separate parts (denoted by I_1 and I_2), for both Newtonian and viscoelastic jets. On the I_1 branch, the real parts of the eigenvalues on the centreline approach the dimensionless velocity of the internal fluid (i.e. the phase speed $c_r \approx 1$), which means that the I_1 branch is related to the internal fluid. While for the I_2 branch, the real parts of most eigenvalues are concentrated near the dimensionless velocity of the external gas (i.e. $c_r \approx Q^{-1/2} \approx 27$), so the I_2 branch is related to the external gas. For the I_2 branch, a characteristic ‘Y-shaped’ structure can be observed, which is well known for Poiseuille flow of a Newtonian fluid (Schmid & Henningson 2001). In contrast to the case of Newtonian jets, a ring structure appears on the I_1 branch for the low El in viscoelastic spectra. Similar to the cases of viscoelastic plane and pipe flows, the ring structure originates from the discrete high-frequency Gorodtsov–Leonov modes (refer to Chaudhary *et al.* 2021). This demonstrates the viscoelastic jet spectrum

Instability of viscoelastic jet in co-flowing gas stream

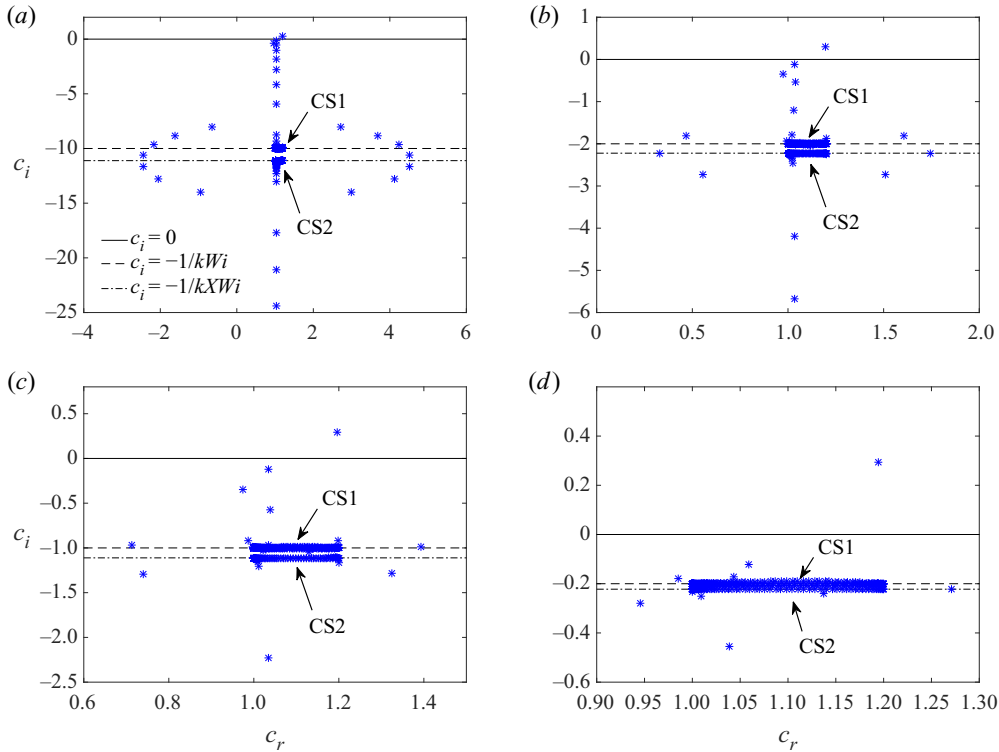


Figure 14. Eigenspectra of the jet for an Oldroyd-B fluid at $k = 1$, $Re = 100$, $We = 3$, $X = 0.9$, $Q = 0.0013$, $N = 0.018$, $U_s = 1.2$ and $K = 0.9$, with El ranging from 1×10^{-3} to 0.05 (equivalently, Wi ranging from 0.1 to 5): (a) $El = 1 \times 10^{-3}$ ($Wi = 0.1$); (b) $El = 5 \times 10^{-3}$ ($Wi = 0.5$); (c) $El = 0.01$ ($Wi = 1$) and (d) $El = 0.05$ ($Wi = 5$). The eigenspectra are obtained using $N_1 = 200$ and $N_2 = 120$. Here, we concentrate on showing the change of the ring structure on the I_1 branch, since there is no obvious change of the ‘Y-shaped’ structure of the I_2 branch. The ring structure is prominent at the lower El , but is absent beyond $El \sim 10^{-2}$ or $Wi \sim 1$. The locations of the CS1 and CS2 lines are shown for reference, where $c_i = -1/kWi$ and $-1/kXWi$, respectively, and $c_r \in [\min\{U_1\}, \max\{U_1\}] = [1, 1.2]$ (note that $U_s = 1.2$) for the two CS. The eigenvalue with $c_i > 0$ is the unstable one.

differs substantially from its Newtonian counterpart. As El is increased from 10^{-4} to 10^{-3} (Wi from 0.01 to 0.1), the ring structure gets smaller in size (see figure 16). Interestingly, for Jeffreys viscoelastic jets, the ring falls off from the I_1 branch with the increase of El , in contrast with the case of Oldroyd-B viscoelastic jets (figure 16).

With increasing El (ranging from 10^{-3} to 0.05) or equivalently Wi (ranging from 0.1 to 5) for a fixed Re , figure 14 shows the ring structure of the viscoelastic spectrum is altered in a singular manner. Meanwhile, a visible feature is the appearance of two continuous spectra (CS) located in the centre of the ring structure. It is now well understood that the CS arise from the local nature of the constitutive model for the polymeric stress (Graham 1998; Chaudhary *et al.* 2021; Roy *et al.* 2021). Specifically, the origin of the CS in viscoelastic flows can be traced to the singularity which arises when the coefficient of the highest-order derivative in the differential equation governing the stability vanishes. Similar to the cases of viscoelastic plane and pipe flows (Chaudhary *et al.* 2021; Khalid *et al.* 2021), this coefficient turns out to be the product $[1 + ikWi(U_1 - c)][1 + ikXWi(U_1 - c)]$. This leads to a pair of horizontal ‘lines’ in the $c_r - c_i$ plane with $c_i = -1/kWi$ and $c_i = -1/kXWi$, respectively, and with $\min\{U_1\} \leq c_r \leq \max\{U_1\}$ for the

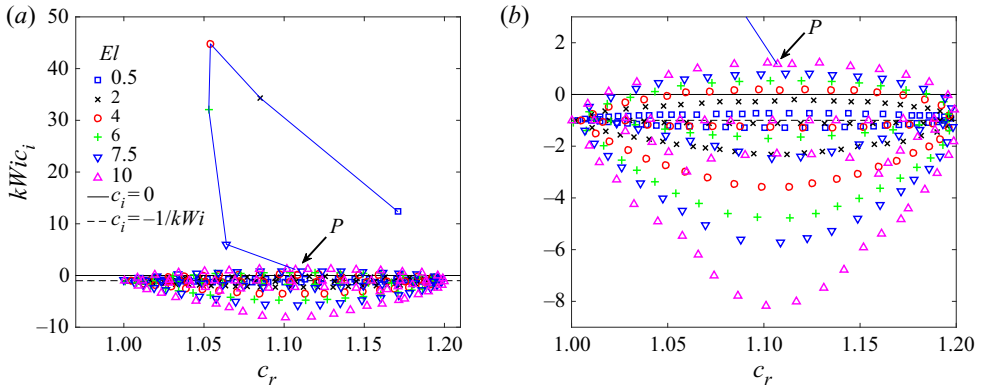


Figure 15. Eigenspectra for the Oldroyd-B fluid for different El in the range 0.5–10, where $k = 1$, $Re = 100$, $We = 3$, $X = 0.9$, $Q = 0.0013$, $N = 0.018$, $U_s = 1.2$ and $K = 0.9$. The eigenspectra are obtained using $N_1 = 200$ and $N_2 = 120$. The scaled growth rate $kWi c_i$ fixes the locations of both the CS (for $X = 0.9$, CS1 and CS2 lie very close to each other). The continuous (blue) line in (a) shows the trajectory of the most unstable eigenvalue as El is varied. The ranges of c_r and c_i are chosen so as to provide a larger view of the part of interest. (b) Enlarged region where the most unstable eigenvalue collapses into the CS balloon at the point P.

two CS. Henceforth, these two continuous spectra are respectively abbreviated as ‘CS1’ and ‘CS2’, where CS1 with $c_i = -1/kWi$ is present even in the absence of solvent (i.e. $X = 0$) and CS2 with $c_i = -1/kXWi$ is present only for a non-zero X .

The ring surrounds the continuous spectra at small El of $O(\sim 10^{-3})$. As Wi or El is increased, both CS1 and CS2 get closer to zero, and at the same time, the ring moves towards the CS with the ring getting smaller in size (figures 14(a) and 14(b)). Note that the size of the CS (i.e. the range of c_r) is constant. For $El \sim 10^{-2}$ (i.e. $Wi \sim 1$), the ring structure is distorted and for higher El (Wi) the modes originally on the ring collapse into the CS in an irregular manner (figure 14d). Since Wi quantifies the nonlinear response of viscoelastic fluids (Galindo-Rosales *et al.* 2014; Ding & Jian 2021), we conclude that the ring structure, existing when $Wi < O(1)$, is related to the linear properties of fluid elasticity. When the nonlinearity of fluid elasticity dominates, characterized by $Wi > O(1)$, the ring structure disappears while the CS become prominent. In contrast, the CS do not appear for Jeffreys fluids due to the linear constitutive relation in (2.5) (see figure 16). Note that the eigenvalues in the ring and CS correspond to stable modes. The variations of unstable eigenvalues and the corresponding growth rates and phase speeds have been explored in detail in §§ 4.1 and 4.2, respectively.

Figure 15 displays the eigenspectra for El ranging from 0.5 to 10, where the scaled growth rate $kWi c_i$ is used to fix the locations of the CS and the ranges of c_r and c_i are chosen so as to provide a larger view of the part of interest. For this range of El , the CS are very close to zero ($c_i = -2 \times 10^{-2} \sim -10^{-3}$). As the eigenfunctions corresponding to the CS eigenvalues are singular, the spectral method, using a finite number of polynomials to approximate the dynamical variables, does not resolve the singular eigenfunctions as accurately as those corresponding to the discrete eigenvalues, which results in a ballooning up of the (expected) ‘line’ of eigenvalues. The spread of the CS balloon only decreases slowly with increasing the collocation points. The continuous line in figure 15(a) represents the trajectory of the most unstable eigenvalue as El is varied, from which one can see that the most unstable eigenvalue eventually fall into the CS balloon as El increases to 10 (i.e. $(1 - X)El = 1$). This leads to a sharp deterioration in the accuracy

Instability of viscoelastic jet in co-flowing gas stream

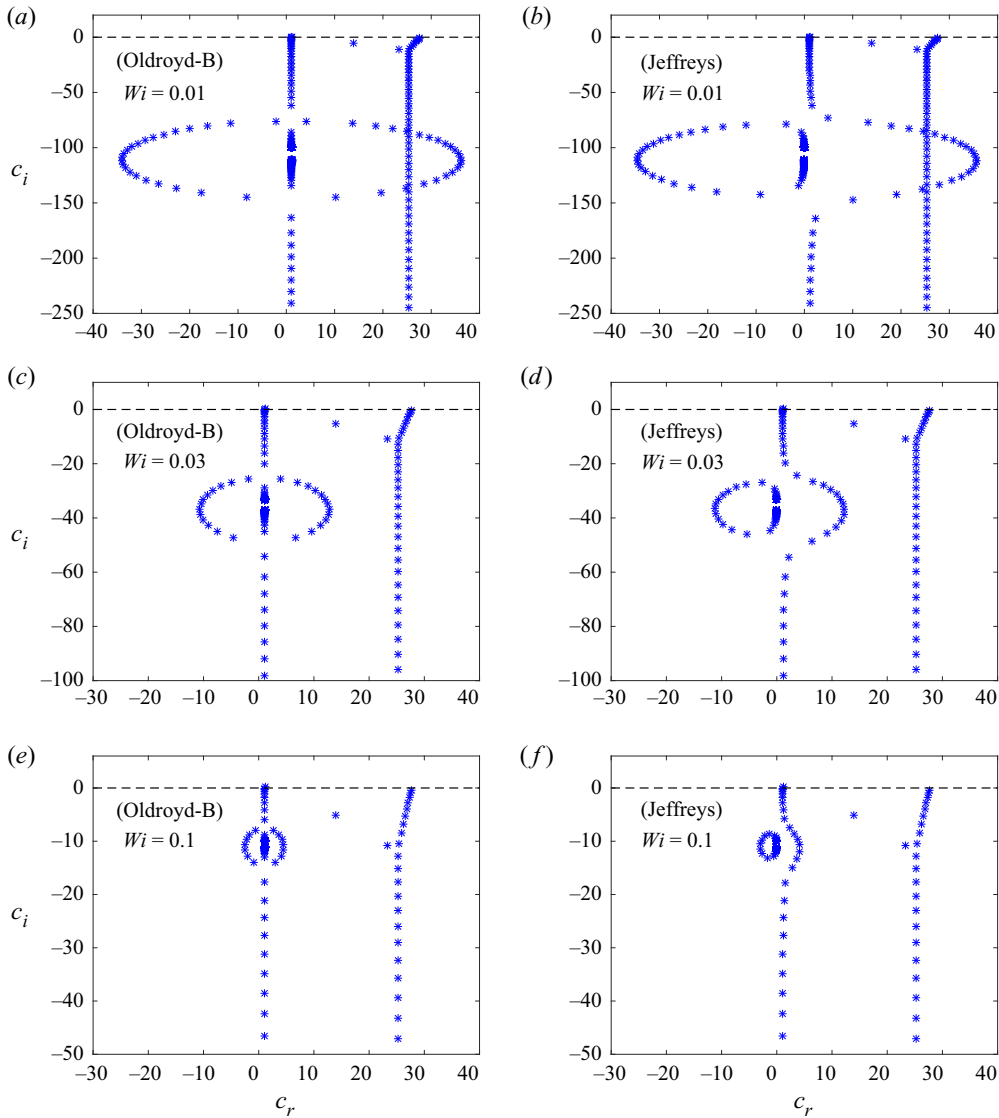


Figure 16. Eigenspectra of the jet for Oldroyd-B fluids with (a) $El = 1 \times 10^{-4}$ ($Wi = 10^{-2}$), (c) $El = 3 \times 10^{-4}$ ($Wi = 3 \times 10^{-2}$) and (e) $El = 1 \times 10^{-3}$ ($Wi = 0.1$) and for Jeffreys fluids with (b) $El = 1 \times 10^{-4}$, (d) $El = 3 \times 10^{-4}$ and (f) $El = 1 \times 10^{-3}$, at $k = 1$, $X = 0.9$, $Re = 100$, $We = 3$, $Q = 0.0013$, $N = 0.018$, $U_s = 1.2$, $K = 0.9$. In order to ensure accuracy, the eigenspectra are obtained using $N_1 = 120$ and $N_2 = 100$. Note that the ranges of c_r and c_i are chosen so as to provide a larger view of the spectra.

and convergence for resolving the most unstable eigenvalue at $El \sim 10$ or more generally $(1 - X)El \sim 1$. For this reason, we restrict to $(1 - X)El < 1$ in this work.

Finally, we compare the evolution of the eigenspectra of Jeffreys and Oldroyd-B viscoelastic jets with the same parameters in figure 16. It can be observed that for the case of Oldroyd-B fluids, the ring structure becomes smaller in size with the increase of El but it remains on the I_1 branch. In contrast, for Jeffreys fluids, the ring structure not only becomes smaller in size, but also it gradually separates from the I_1 branch with the increase of El .

For Oldroyd-B fluids, the ring structure disappears while the continuous spectra become visible at $Wi \sim 1$ (figure 14). In contrast, for Jeffreys fluids, the ring structure only shrinks further but not disappear with the increase of Wi ($Wi \gg 1$), and no continuous spectra appear. This verifies that the ring structure is related to the linear behaviour of fluid elasticity, whereas the appearance of the continuous spectra is related to the nonlinear behaviour of fluid elasticity.

REFERENCES

- ALSHARIF, A.M., UDDIN, J. & AFZAAL, M.F. 2015 Instability of viscoelastic curved liquid jets. *Appl. Math. Model.* **39** (14), 3924–3938.
- BARRERO, A. & LOSCERTALES, I.G. 2007 Micro- and nanoparticles via capillary flows. *Annu. Rev. Fluid Mech.* **39**, 89–106.
- BASARAN, O.A., GAO, H. & BHAT, P.P. 2013 Nonstandard inkjets. *Annu. Rev. Fluid Mech.* **45**, 85–113.
- BIRD, R.B., ARMSTRONG, R.C. & HASSAGER, O. 1987 *Dynamics of Polymeric Liquids, vol. 1. Fluid Mechanics*, 2nd edn. Wiley.
- BOYD, J.P. 1999 *Chebyshev and Fourier Spectral Methods*, 2nd edn. Springer.
- BRENN, G., LIU, Z. & DURST, F. 2000 Linear analysis of the temporal instability of axisymmetrical non-Newtonian liquid jets. *Intl J. Multiphase Flow* **26** (10), 1621–1644.
- CHANDRASEKHAR, S. 1961 *Hydrodynamic and Hydromagnetic Stability*. Oxford University Press.
- CHAUDHARY, I., GARG, P., SUBRAMANIAN, G. & SHANKAR, V. 2021 Linear instability of viscoelastic pipe flow. *J. Fluid Mech.* **908**, A11.
- DING, Z. & JIAN, Y. 2021 Electrokinetic oscillatory flow and energy conversion of viscoelastic fluids in microchannels: a linear analysis. *J. Fluid Mech.* **919**, A20.
- EGGERS, J., HERRADA, M.A. & SNOEIJER, J.H. 2020 Self-similar breakup of polymeric threads as described by the Oldroyd-B model. *J. Fluid Mech.* **887**, A19.
- EGGERS, J. & VILLERMAUX, E. 2008 Physics of liquid jets. *Rep. Prog. Phys.* **71**, 036601.
- GALINDO-ROSALES, F.J., CAMPO-DEAÑO, L., SOUSA, P.C., RIBEIRO, V.M. & PINHO, F.T. 2014 Viscoelastic instabilities in micro-scale flows. *Expl Therm. Fluid Sci.* **59**, 128–139.
- GAÑÁN-CALVO, A.M. 1998 Generation of steady liquid microthreads and micron-sized monodisperse sprays in gas streams. *Phys. Rev. Lett.* **80** (2), 285–288.
- GAÑÁN-CALVO, A.M., MONTANERO, J.M., MARTÍN-BANDERAS, L. & FLORES-MOSQUERA, M. 2013 Building functional materials for health care and pharmacy from microfluidic principles and flow focusing. *Adv. Drug Deliv. Rev.* **65**, 1447–1469.
- GAÑÁN-CALVO, A.M. & RIESCO-CHUECA, P. 2006 Jetting–dripping transition of a liquid jet in a lower viscosity co-flowing immiscible liquid: the minimum flow rate in flow focusing. *J. Fluid Mech.* **553**, 75–84.
- GARG, P., CHAUDHARY, I., KHALID, M., SHANKAR, V. & SUBRAMANIAN, G. 2018 Viscoelastic pipe flow is linearly unstable. *Phys. Rev. Lett.* **121** (2), 024502.
- GOLDIN, M., YERUSHALMI, J., PFEFFER, R. & SHINNAR, R. 1969 Breakup of a laminar capillary jet of a viscoelastic fluid. *J. Fluid Mech.* **38** (4), 689–711.
- GORDILLO, J.M., PÉREZ-SABORID, M. & GAÑÁN-CALVO, A.M. 2001 Linear stability of co-flowing liquid–gas jets. *J. Fluid Mech.* **448**, 23–51.
- GORDON, M., YERUSHALMI, J. & SHINNAR, R. 1973 Instability of jets of non-Newtonian fluids. *J. Rheol.* **17** (2), 303–324.
- GOREN, S.L. & GOTTLIEB, M. 1982 Surface-tension-driven breakup of viscoelastic liquid threads. *J. Fluid Mech.* **120**, 245–266.
- GRAHAM, M.D. 1998 Effect of axial flow on viscoelastic Taylor–Couette instability. *J. Fluid Mech.* **360**, 341–374.
- GUERRERO, J., CHANG, Y.-W., FRAGKOPOULOS, A.A. & FERNANDEZ-NIEVES, A. 2020 Capillary-based microfluidics–coflow, flow-focusing, electro-coflow, drops, jets, and instabilities. *Small* **16** (9), 1904344.
- HERRADA, M.A., MONTANERO, J.M., FERRERA, C. & GAÑÁN-CALVO, A.M. 2010 Analysis of the dripping–jetting transition in compound capillary jets. *J. Fluid Mech.* **649**, 523–536.
- JAMES, D.F. 2009 Boger fluids. *Annu. Rev. Fluid Mech.* **41**, 129–142.
- JOSEPH, D.D. & RENARDY, Y.Y. 1992 *Fundamentals of Two-Fluid Dynamics*. Springer.
- KHALID, M., CHAUDHARY, I., GARG, P., SHANKAR, V. & SUBRAMANIAN, G. 2021 The centre-mode instability of viscoelastic plane poiseuille flow. *J. Fluid Mech.* **915**, A43.
- KROESSER, F.W. & MIDDLEMAN, S. 1969 Viscoelastic jet stability. *AIChE J.* **15** (3), 383–386.
- LARSON, R.G. 1988 *Constitutive Equations for Polymer Melts and Solutions*. Butterworths.

Instability of viscoelastic jet in co-flowing gas stream

- LARSON, R.G. 1992 Instabilities in viscoelastic flows. *Rheol. Acta* **31** (3), 213–263.
- LI, F., KE, S.-Y., YIN, X.-Y. & YIN, X.-Z. 2019 Effect of finite conductivity on the nonlinear behaviour of an electrically charged viscoelastic liquid jet. *J. Fluid Mech.* **874**, 5–37.
- LI, F., YIN, X.-Y. & YIN, X.-Z. 2011 Axisymmetric and non-axisymmetric instability of an electrically charged viscoelastic liquid jet. *J. Non-Newtonian Fluid Mech.* **166** (17–18), 1024–1032.
- LIN, S.P. 2003 *Breakup of Liquid Sheets and Jets*. Cambridge University Press.
- LIN, S.P. & CHEN, J.N. 1998 Role played by the interfacial shear in the instability mechanism of a viscous liquid jet surrounded by a viscous gas in a pipe. *J. Fluid Mech.* **376**, 37–51.
- LIN, S.P. & IBRAHIM, E.A. 1990 Instability of a viscous liquid jet surrounded by a viscous gas in a vertical pipe. *J. Fluid Mech.* **218**, 641–658.
- LIU, Z. & LIU, Z. 2006 Linear analysis of three-dimensional instability of non-Newtonian liquid jets. *J. Fluid Mech.* **559**, 451–459.
- LIU, Z. & LIU, Z. 2008 Instability of a viscoelastic liquid jet with axisymmetric and asymmetric disturbances. *Intl J. Multiphase Flow* **34** (1), 42–60.
- MIDDLEMAN, S. 1965 Stability of a viscoelastic jet. *Chem. Engng Sci.* **20** (12), 1037–1040.
- MOHAMED, A.S., HERRADA, M.A., GAÑÁN-CALVO, A.M. & MONTANERO, J.M. 2015 Convective-to-absolute instability transition in a viscoelastic capillary jet subject to unrelaxed axial elastic tension. *Phys. Rev. E* **92** (2), 023006.
- MONTANERO, J.M. & GAÑÁN-CALVO, A.M. 2008 Viscoelastic effects on the jetting–dripping transition in co-flowing capillary jets. *J. Fluid Mech.* **610**, 249–260.
- MONTANERO, J.M. & GAÑÁN-CALVO, A.M. 2020 Dripping, jetting and tip streaming. *Rep. Prog. Phys.* **83** (9), 097001.
- MOROZOV, A.N. & VAN SAARLOOS, W. 2007 An introductory essay on subcritical instabilities and the transition to turbulence in visco-elastic parallel shear flows. *Phys. Rep.* **447** (3–6), 112–143.
- MU, K., QIAO, R., SI, T., CHENG, X. & DING, H. 2021 Interfacial instability and transition of jetting and dripping modes in a co-flow focusing process. *Phys. Fluids* **33** (5), 052118.
- OTTO, T., ROSSI, M. & BOECK, T. 2013 Viscous instability of a sheared liquid-gas interface: dependence on fluid properties and basic velocity profile. *Phys. Fluids* **25** (3), 032103.
- PAGE, J. & ZAKI, T.A. 2016 Viscoelastic shear flow over a wavy surface. *J. Fluid Mech.* **801**, 392–429.
- PONCE-TORRES, A., MONTANERO, J.M., VEGA, E.J. & GAÑÁN-CALVO, A.M. 2016 The production of viscoelastic capillary jets with gaseous flow focusing. *J. Non-Newtonian Fluid Mech.* **229**, 8–15.
- QIAO, R., MU, K., LUO, X. & SI, T. 2020 Instability and energy budget analysis of viscous coaxial jets under a radial thermal field. *Phys. Fluids* **32** (12), 122103.
- RAYLEIGH, L. 1878 On the instability of jets. *Proc. Lond. Math. Soc.* **10**, 4–13.
- ROSELL-LLOMPART, J. & GAÑÁN-CALVO, A.M. 2008 Turbulence in pneumatic flow focusing and flow blurring regimes. *Phys. Rev. E* **77** (3), 036321.
- ROY, A., GARG, P., REDDY, J.S. & SUBRAMANIAN, G. 2021 Inertio-elastic instability of a vortex column. [arXiv:2101.00805](https://arxiv.org/abs/2101.00805).
- RUO, A.-C., CHEN, F., CHUNG, C.-A. & CHANG, M.-H. 2011 Three-dimensional response of unrelaxed tension to instability of viscoelastic jets. *J. Fluid Mech.* **682**, 558–576.
- SCHMID, P.J. & HENNINGSON, D.S. 2001 *Stability and Transition in Shear Flows*. Springer.
- SEVILLA, A., GORDILLO, J.M. & MARTÍNEZ-BAZÁN, C. 2002 The effect of the diameter ratio on the absolute and convective instability of free co-flowing jets. *Phys. Fluids* **14** (9), 3028–3038.
- SI, T., LI, F., YIN, X.-Y. & YIN, X.-Z. 2009 Modes in flow focusing and instability of coaxial liquid–gas jets. *J. Fluid Mech.* **629**, 1–23.
- TAYLOR, G.I. 1962 Generation of ripples by wind blowing over a viscous fluid. In *The Scientific Papers of G.I. Taylor* (ed. G.K. Batchelor), pp. 244–254. Cambridge University Press.
- WEBER, C. 1931 On the breakdown of a fluid jet. *Z. Angew. Math. Mech.* **11**, 136–141.
- WEIDEMAN, J.A. & REDDY, S.C. 2000 A matlab differentiation matrix suite. *ACM Trans. Math. Softw.* **26** (4), 465–519.
- WHITE, F.M. 1998 *Fluid Mechanics*, 4th edn, pp. 231–233. McGraw-Hill.
- XIE, L., YANG, L.-J., FU, Q.-F. & QIN, L.-Z. 2016 Effects of unrelaxed stress tension on the weakly nonlinear instability of viscoelastic sheets. *Phys. Fluids* **28** (10), 104104.
- YE, H.-Y., YANG, L.-J. & FU, Q.-F. 2016 Instability of viscoelastic compound jets. *Phys. Fluids* **28** (4), 043101.
- YECKO, P., ZALESKI, S. & FULLANA, J.M. 2002 Viscous modes in two-phase mixing layers. *Phys. Fluids* **14** (12), 4115–4122.